SEISMIC COUPLING FROM A NUCLEAR EXPLOSION
THE DEPENDENCE OF THE REDUCED DISPLACEMENT
POTENTIAL ON THE NONLINEAR BEHAVIOR OF THE
NEAR SOURCE ROCK ENVIRONMENT

Systems, Science and Software
La Jolla, California

September 1975

006225

SYSTEMS, SCIENCE AND SOFTWARE

SEISMIC COUPLING FROM A NUCLEAR EXPLOSION:
THE DEPENDENCE OF THE REDUCED DISPLACEMENT POTENTIAL
ON THE NONLINEAR BEHAVIOR OF THE NEAR SOURCE ROCK
ENVIRONMENT

J. T. Cherry
N. Rimer
W. O. Wray

Technical Report

The views and conclusions contained in this docu-
ment are those of the authors and should not be
interpreted as necessarily representing the
official policies, either expressed or implied,
of the Advanced Research Projects Agency, the
Air Force Technical Applications Center, or the
U. S. Government.

September 1975

AFTAC Project Authorization No. VELA T/6712/B/ETR

ARPA Order No. 2551   Contract No. F08606-75-C-0045

Contractor: Systems, Science and Software
              P. O. Box 1620
              La Jolla, California 92038

Effective Date of Contract: May 1, 1975

Contract Expiration Date: September 30, 1976

Principal Investigator and Phone No.

       Dr. John M. Savino (714) 453-0060, Ext. 455

Project Scientist and Phone No.

       Dr. Ralph W. Alewine, III (703) 325-8484

Short Title of Work:

       Seismic Coupling from Nuclear Explosion

Amount of Contract: $448,250

Contract Period Covered by Report: N/A

SECURITY CLASSIFICATION OF THIS PAGE (When Data Entered)

REPORT DOCUMENTATION PAGE	READ INSTRUCTIONS BEFORE COMPLETING FORM

1. REPORT NUMBER	2. GOVT ACCESSION NO.	3. RECIPIENT'S CATALOG NUMBER

4. TITLE (and Subtitle)	5. TYPE OF REPORT & PERIOD COVERED
SEISMIC COUPLING FROM A NUCLEAR EXPLOSION: THE DEPENDENCE OF THE REDUCED DISPLACEMENT POTENTIAL ON THE NONLINEAR BEHAVIOR OF THE NEAR SOURCE ROCK ENVIRONMENT	Topical Report, 9/75
	6. PERFORMING ORG. REPORT NUMBER
	SSS-R-76-2742

7. AUTHOR(s)	8. CONTRACT OR GRANT NUMBER(s)
J. T. Cherry, N. Rimer and W. O. Wray	Contract No. F08606-75-C-0045

9. PERFORMING ORGANIZATION NAME AND ADDRESS	10. PROGRAM ELEMENT, PROJECT, TASK AREA & WORK UNIT NUMBERS
Systems, Science and Software P. O. Box 1620 La Jolla, CA 92038	Program Code No. 6F10 ARPA Order No. 2551

11. CONTROLLING OFFICE NAME AND ADDRESS	12. REPORT DATE
VELA Seismological Center 312 Montgomery Street Alexandria, VA 22314	Sept. 1975
	13. NUMBER OF PAGES
	83

14. MONITORING AGENCY NAME & ADDRESS(if different from Controlling Office)	15. SECURITY CLASS. (of this report)
	Unclassified
	15a. DECLASSIFICATION/DOWNGRADING SCHEDULE

16. DISTRIBUTION STATEMENT (of this Report)

Approved for public release; distribution unlimited

17. DISTRIBUTION STATEMENT (of the abstract entered in Block 20, if different from Report)

18. SUPPLEMENTARY NOTES

19. KEY WORDS (Continue on reverse side if necessary and identify by block number)

Underground Nuclear Explosions   Body Wave Magnitude
Constitutive Modeling   Earth Structure
Seismic Coupling
Reduced Displacement Potential

20. ABSTRACT (Continue on reverse side if necessary and identify by block number)

The objective of the research presented in this report is to determine the dependence of teleseismic magnitudes on the nonlinear behavior of the near source rock environment. Such information enables one to express uncertainties in explosive yield estimates in terms of uncertainties in the material properties and provides insight concerning the requirements for collection of geophysical data at a specific test site.

DD FORM 1473   EDITION OF 1 NOV 65 IS OBSOLETE
1 JAN 73

A series of spherically symmetric calculations have been performed in which the properties of the near source material were varied systematically. Output from these calculations enables one to determine the relative teleseismic coupling efficiency of a given near source material. Also, since seismic magnitudes are directly related to explosive yield, this parameter study permits an assessment of uncertainties in the estimated yield in terms of uncertainties of the material properties of the test site.

TABLE OF CONTENTS

SUMMARY

During the past several years, Systems, Science and Software (S³) personnel have been actively engaged in a comprehensive program involving computer modeling of the non-linear processes that characterize the near source ground motion from underground nuclear explosions, propagation of the resultant stress waves through the crust and upper mantle and prediction of the ground motion recorded at teleseismic distances from the explosion [Cherry, et al. (1973), Bache, et al. (1975)].

The objective of the research presented in this report is to determine the dependence of teleseismic magnitudes on the nonlinear behavior of the near source rock environment. Such information enables one to express uncertainties in explosive yield estimates in terms of uncertainties in the material properties and provides insight concerning the requirements for collection of geophysical data at a specific test site.

A series of spherically symmetric calculations have been performed in which the properties of the near source material were varied systematically. Output from these calculations enables one to determine the relative teleseismic coupling efficiency of a given near source material. Also, since seismic magnitudes are directly related to explosive yield, this parameter study permits an assessment of uncertainties in the estimated yield in terms of uncertainties of the material properties of the test site.

I.   INTRODUCTION

1.1   OBJECTIVES

This report describes the results of a theoretical study directed at the determination of the sensitivity of the equivalent elastic source from a nuclear explosion to the nonlinear behavior of the near source rock environment. Uncertainties in yield estimates based on measured seismic magnitudes may be expressed in terms of uncertainties in the near source properties. The material parameters and the aspects of the constitutive model which have the greatest effect on the equivalent source are identified and guidelines are established for the collection of geophysical data in the near source region.

1.2   PROCEDURE

Equivalent elastic source calculations place severe requirements on both the constitutive model and the stress wave simulation code which contains the model. The constitutive model must account for the various modes of material behavior which occur between the cavity boundary and the distance at which the material response is elastic. The stress wave code must not only be able to easily accept the constitutive model but also accurately propagate the stress wave into the elastic region. The equivalent elastic source is then obtained from the properties of the displacement field in the elastic region.

Constitutive models, especially that portion of the model which pertains to the material strength, can be fairly complex. In order to isolate the effect of the constitutive model on seismic coupling we first assumed that only plastic flow would result when the allowable material strength was exceeded and an extensive parameter study was completed for

a water-tuff rock environment containing various amounts of air-filled porosity. We then modified the strength portion of the constitutive model to simulate tension failure, shear failure and the role of pore fluid pressure on effective stress.

Figure 1.1 depicts, in flow chart form, the organization of the parameter study. The material selected consists of a mixture of tuff and water which may contain air-filled voids. The properties of the water and grain density tuff constituents were held constant for all calculations. The mass fraction of water in the mixture, f_w, is a natural parameter to select for initial variation and this choice is indicated in Fig. 1.1; the air-filled volume fraction, ϕ_0, was set to zero for this set of calculations. The equation of state for the tuff-water mixture is described in Section 2.1 of this report.

The remaining material parameters are varied one at a time while holding the water mass fraction constant at 0.17. Four of the material parameters are directly related to the porosity model which is discussed in Section 2.1: (1) the initial air-filled volume fraction, ϕ_0; (2) the elastic limit of the pressure, P_e; (3) the crush or compaction pressure, P_c; (4) the bulk modulus, k_0. The shear modulus, μ, is selected as one of the independent elastic properties of the porous mixture. Given k_0, μ and the ambient density, ρ_0, the elastic P wave velocity, c, is given by

$$c = \sqrt{\frac{k_0 + \frac{4}{3}\mu}{\rho_0}}$$

while the shear wave velocity, β, is

$$\beta = \sqrt{\frac{\mu}{\rho_0}}$$

Mixture Constituents

Tuff and Water

Mass Fraction
of Water

f_1 f_2 f_3 f_4 f_5

Air-Filled Porosity Parameters
ϕ_0, P_e, P_c, k_0

Rigidity
μ

Strength Parameters for Plastic Flow
Y, Y_{MAX}, P_m
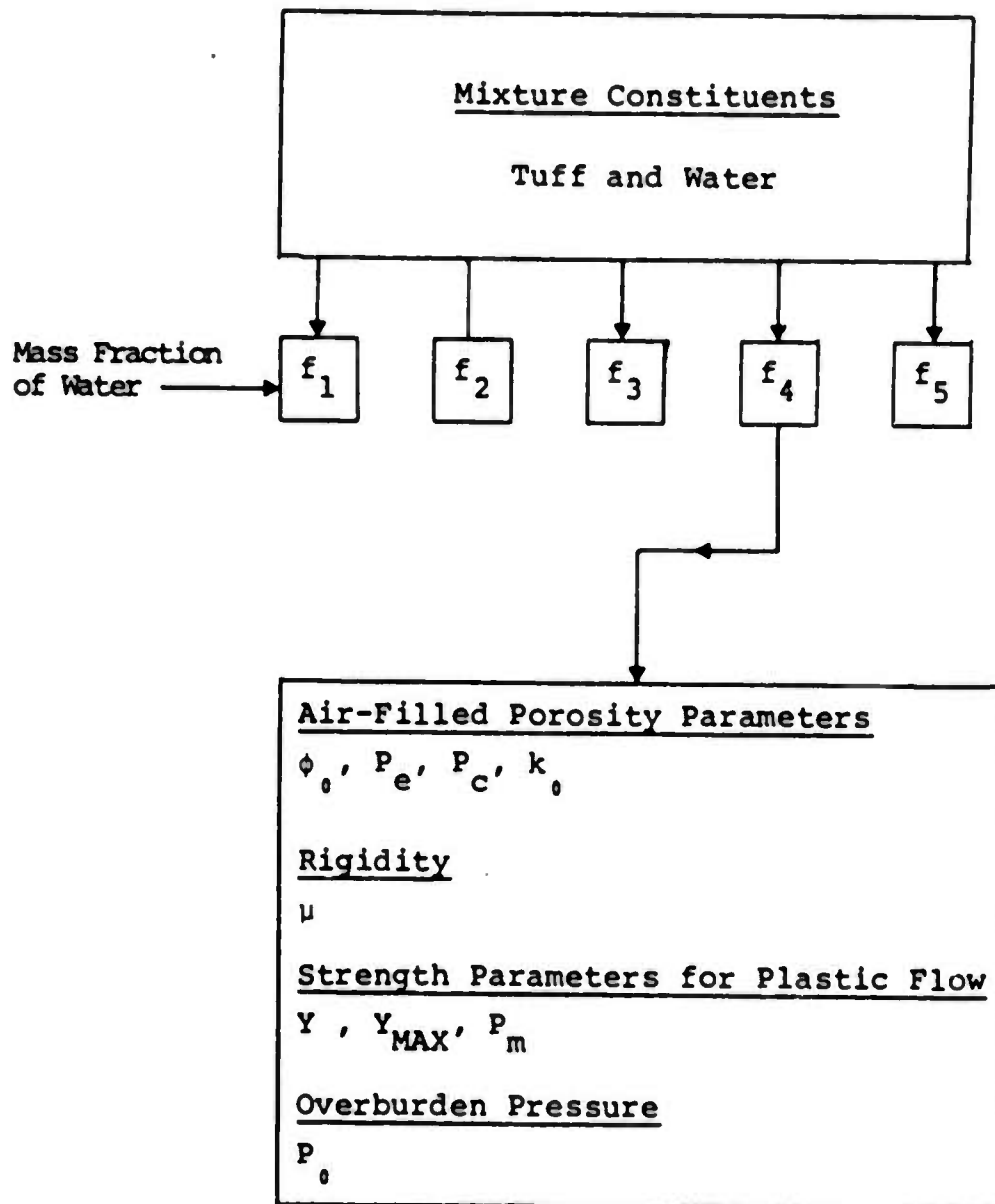
Overburden Pressure
P_0

Figure 1.1.   Flow chart for one-dimensional sensitivity study.

Additional parameters are contained in the material strength model which is discussed in Section 2.2. As noted earlier and shown in Fig. 1.1, only plastic flow was permitted during these calculations. The strength parameters included in this sensitivity study are: (1) the zero pressure yield strength, Y_0; (2) the maximum yield strength, Y_m; (3) the pressure at which the yield strength reaches its maximum value, P_m.

One last parameter, the overburden pressure, P_0, is included in the one-dimensional sensitivity study although it depends on the depth of burial and is not a material property.

A detailed description of the material models employed in our near source calculations is presented in the next section. The results of the sensitivity study are discussed in Section III and conclusions based on those results are summarized in Section IV. In Section V the strength portion of the constitutive model is modified to include tension failure, shear failure and an effective stress law. The shape of the equivalent source spectrum is shown to be strongly dependent on both tension failure and the stress relaxation assumed to result from the effective stress formulation.

II.   DESCRIPTION OF MATERIAL MODELS

For the parameter study we have chosen the rock con-
stituent to be NTS tuff. The following sections, 2.1 and
2.2, present the pressure and material strength formulations
used in the parameter study.

2.1   THE PRESSURE COMPONENT

Given the pressure component of the equation of state
for both water and grain density tuff, then the pressure com-
ponent for a fully saturated mix is obtained by specifying

$$f_w = \frac{M_w}{M_r + M_w} = \text{mass fraction cf water} \qquad (2.1)$$

Figures 2.1 and 2.2 show the Hugoniot and release isentropes
for these two constituents.

At a given pressure $\overline{P}$ a pressure equilibrium mix is
obtained if

$$\overline{v} = \frac{v_r + f' v_w}{1 + f'} \qquad (2.2)$$

$$e = \frac{e_r + f e_w}{1 + f'} \qquad (2.3)$$

where

$$f' = \frac{f_w}{1 - f_w} = \frac{M_w}{M_r} \qquad (2.4)$$

v_r, v_w, e_r and e_w are specific volumes and energies of the
rock and water components of the pressure $\overline{P}$. It is now
possible to generate a table that gives $\overline{P}$ as a function of
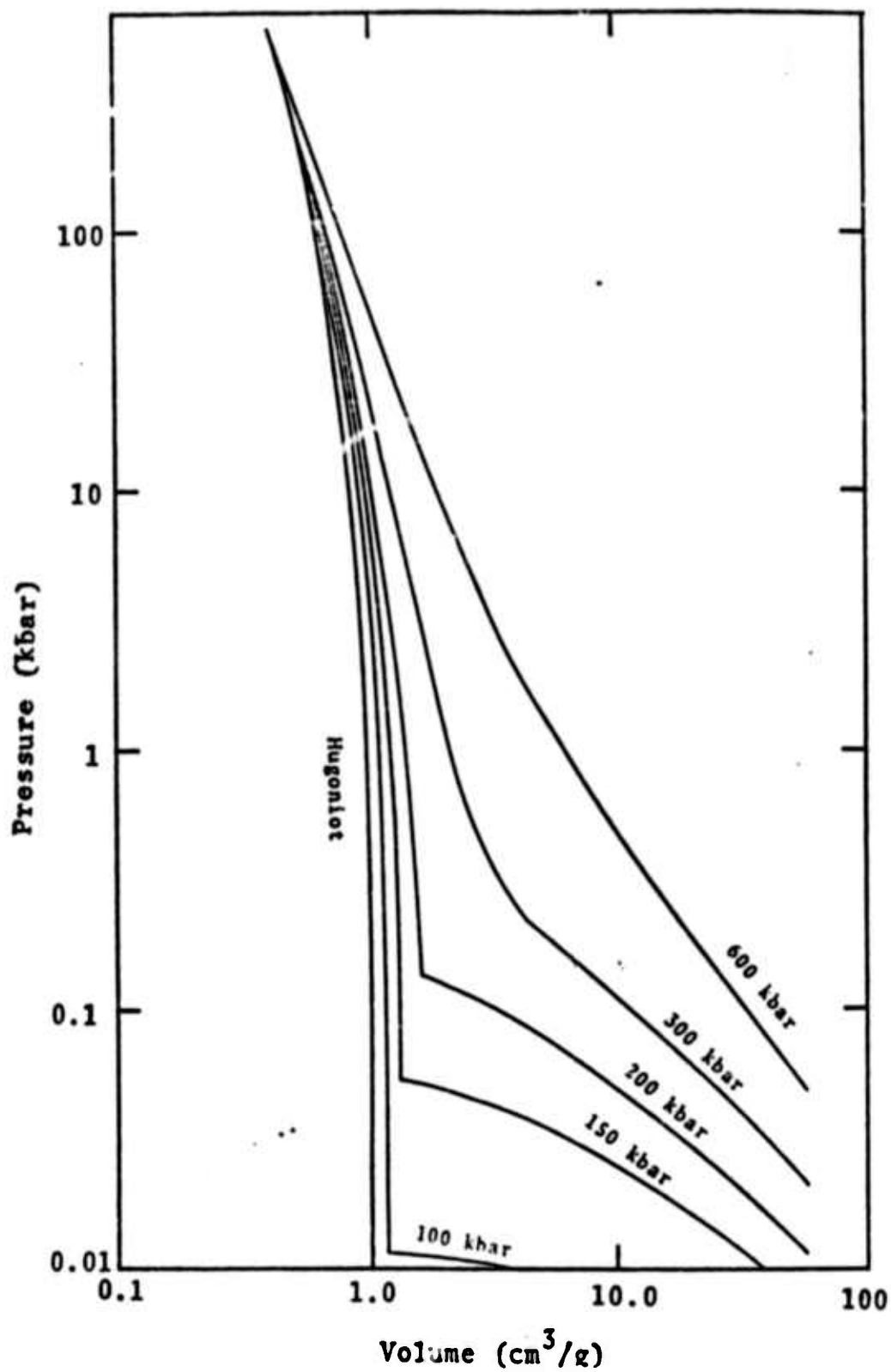
Figure 2.1. Hugoniot and release isentropes for water [Bjork and Gittings (1972)].
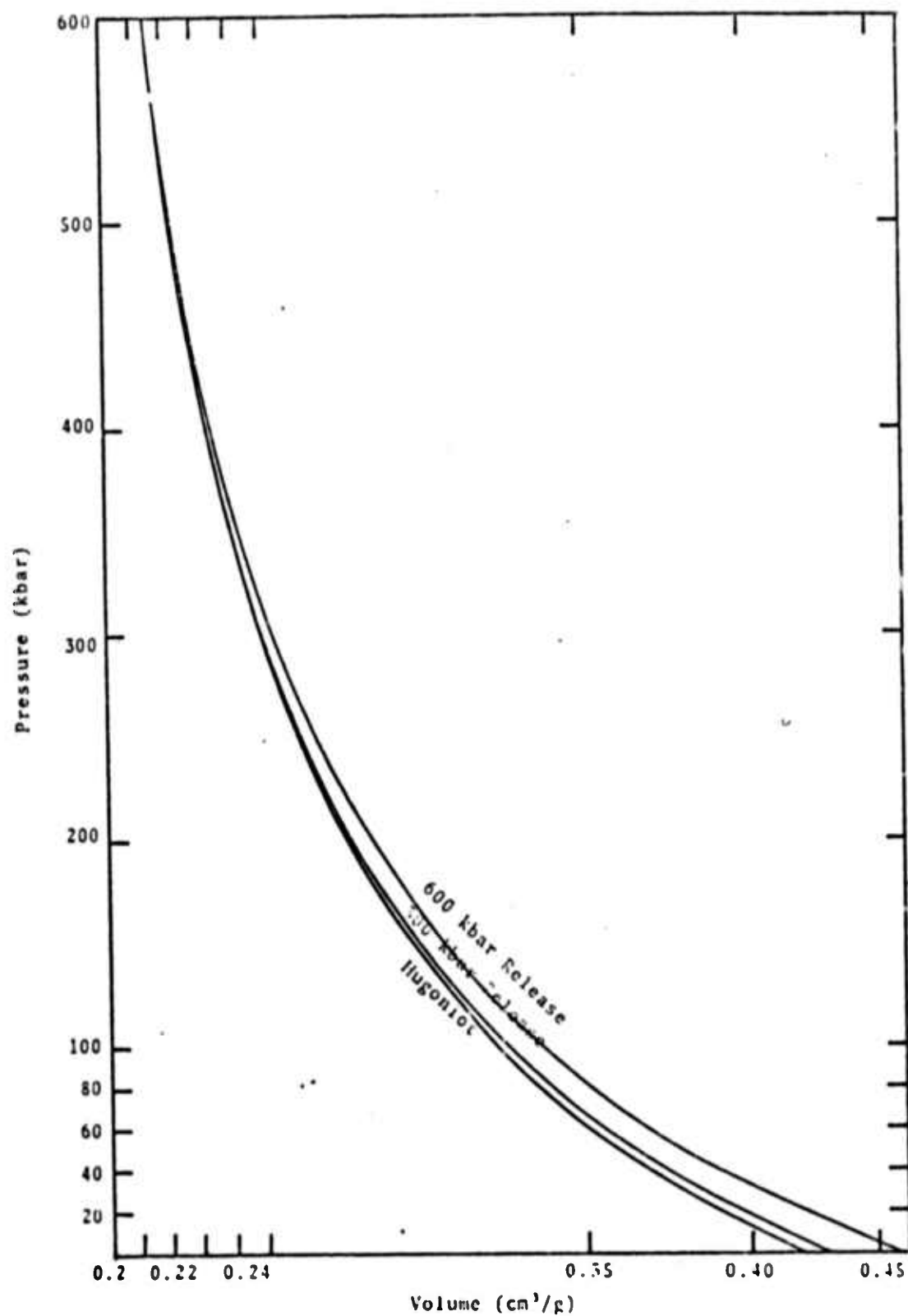
7

Figure 2.2. Hugoniot and release isentropes for tuff, ρ_0 = 2.4 g/cc [Riney, et al. (1972)].

$\bar{v}$ and e. This table (Riney, et al.)[2] suitably chooses values of $\bar{v}$ and e so that no time consuming search is needed when performing an interpolation at a given thermodynamic state. Figure 2.3 shows the result of mixing the rock and water constituents shown in Figs. 2.1 and 2.2 using a 0.17 value for f_w.

Air-filled porosity is included in the model by defining a parameter α, given by

$$\alpha = \frac{V_r + V_w + V_p}{V_r + V_w} = \frac{v}{\bar{v}} \qquad (2.5)$$

where v is the specific volume of the partially saturated mix. Then

$$P = \frac{1}{\alpha} \bar{P} \ (v/\alpha, \ e) \qquad (2.6)$$

where $\bar{P}$ is found from the table using v, e. Equation (2.6) is equivalent to the porosity model proposed by Herrmann (3) except $\bar{P}$ is weighted with $1/\alpha$. Both v and e are zone variables and are obtained from SKIPPER at any given time cycle.

The parameter α is assumed to vary in the following way during loading (pore collapse) [Cherry, et al.][4]

$$\alpha = 1 \qquad P > P_c \qquad (2.7a)$$

$$\alpha = 1 + (\alpha_e - 1)\left(1 - \frac{P-P_e}{P_c - P_e}\right) \qquad P_e \leq P \leq P_c \qquad (2.7b)$$

$$\alpha = \alpha_0 + \beta \left(1 - e^{n \ P/P_e}\right) \qquad 0 \leq P \leq P_e \qquad (2.7c)$$

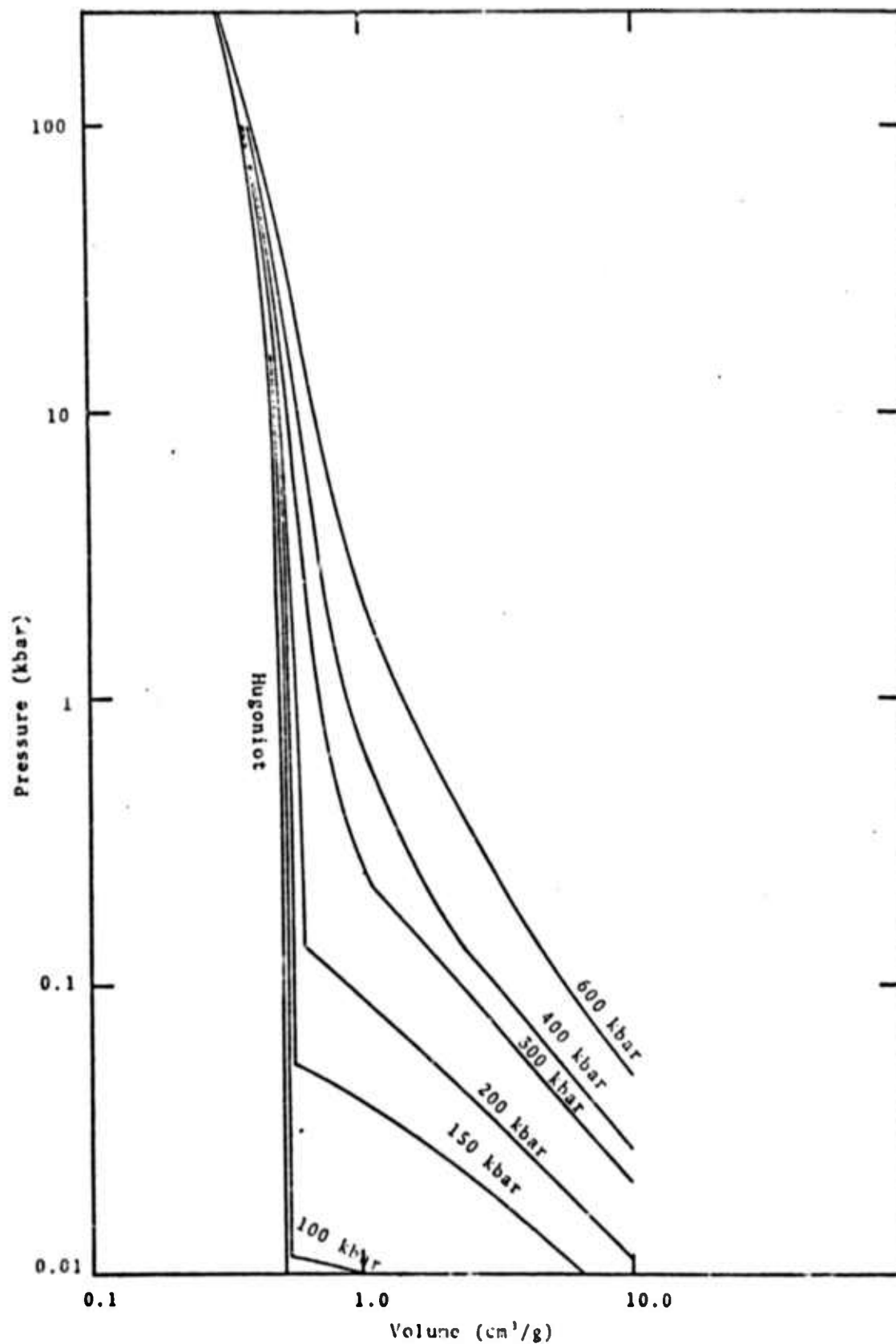$$\alpha = P\alpha'_{P=0} + \alpha_0 \qquad P < 0 \qquad (\alpha' = d\alpha/dp) \qquad (2.7d)$$

Figure 2.3. Hugoniot and release isentropes for saturated tuff (f = 0.17).

where P_e and P_c are the elastic and crush pressure. β and η are determined by specifying the zero pressure bulk modulus (k_0) of the porous mix and requiring that α' be continuous at $P = P_e$. The initial air-filled volume fraction (ϕ_0) and α_0 are related by

$$\phi_0 = \frac{\alpha_0 - 1}{\alpha_0} = \frac{V_p}{V_w + V_r + V_p} \qquad (2.8)$$

while the volume fractions of rock and water (ϕ_r and ϕ_w) are given by

$$\phi_r = \frac{1 - \phi_0}{1 + A} \qquad (2.9)$$

$$\phi_w = \left(\frac{1 - \phi_0}{1 + A} \right) A \qquad (2.10)$$

where

$$A = \frac{\rho_r}{\rho_w} \frac{f}{1-f} \qquad \begin{aligned} \rho_r &= 2.4 \text{ g/cc} \\ \rho_w &= 1.0 \text{ g/cc} \end{aligned}$$

We have found (Cherry, et al.[4]) that a pore recovery formulation needed to be included in the model in order to insure a smooth transition between loading states near P_e. If α^* is the minimum α seen by a zone then

$$\alpha = t\alpha^* + (1-t) \, \alpha \, (P) \qquad (2.11)$$

where (P) is given by Eqs. (2.8) and

$$t = 0, \; \alpha^* \geq \alpha_e = \frac{\alpha^* - \alpha_e}{1 - \alpha_e} , \; 1 \leq \alpha^* \leq_e \qquad (2.12)$$

This assures full recovery when $\alpha^* = \alpha_e$ and zero recovery when $\alpha^* = 1$.

Figure 2.4 shows the loading and release P-v curves
that result from adding 5 percent air-filled porosity to
the mix of Fig. 2.3. We assume $P_e = 0.15$ kbar and $P_c =$
1.25 kbar. Also shown for comparison in the figure are the
hydrostatic unloading data for unit 3 tuff at the Diamond
Dust site (Stephens, et al.[5]).

In summary, the pressure component of the equation of
state is uniquely determined by assuming a pressure equili-
brium mix and specifying f (Eq. (2.1)), ϕ_0 (Eq. (2.8)),
P_e, P_c, k_0 (Eq. (2.7b) and (2.7c)) and the grain density of
the rock component.

2.2 MATERIAL STRENGTH

A strength relation of the form

$$S_{ij} S_{ij} \leq \frac{2}{3} Y^2 (P_T, e) \tag{2.13}$$

where S_{ij} is the stress deviator, $P_T = P + P_0$, P_0 equals
the overburden pressure, and

$$Y(P,e) = \left[Y_0 + Y_m \frac{P}{P_m} (2 - \frac{P}{P_m}) \right] (1 - \frac{e}{e_m}) \quad P < P_m$$

$$= (Y_0 + Y_m) (1 - \frac{e}{e_m}), \quad P \geq P_m \tag{2.14}$$

$$= 0 \quad e \geq e_m$$

For spherical symmetry Eq. (2.13) becomes

$$|S_1| \leq \frac{2}{3} Y (P_T, e) \tag{2.15}$$

For all the calculations performed for the parameter
study, a generalized associated flow rule was used for the
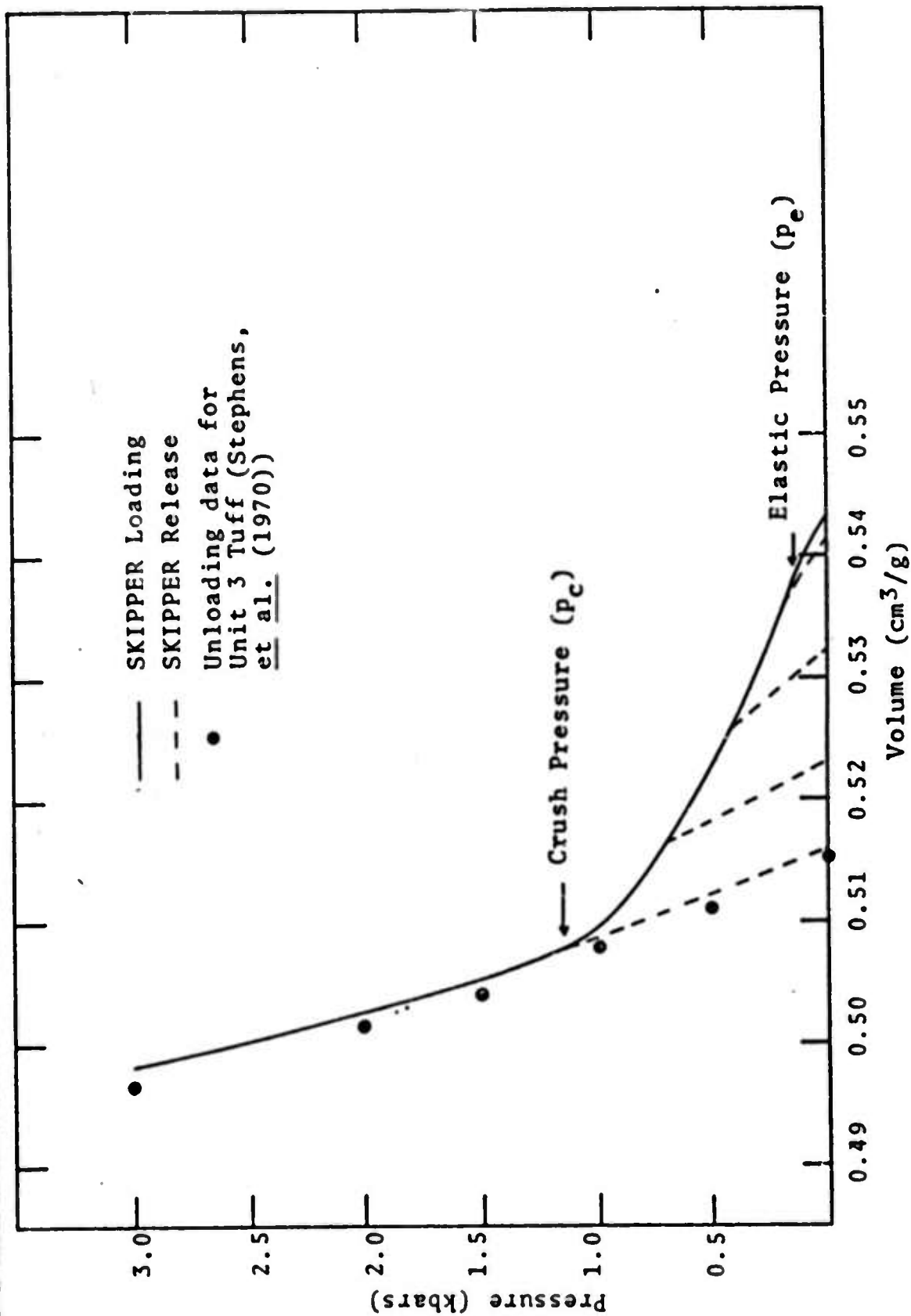material in which the volumetric plastic strain rate was

12

R-2742

Figure 2.4. Loading and release p-V curves for partially saturated tuff (f = 0.17, ϕ_0 = 0.05) [Cherry, et al. (1973)].

13

assumed to be zero. This assumption implies (Cameron and Scorgie[6]) that if $|S_1|$ exceeds $\frac{2}{3}$ Y, then

$$S_1 = \left(\frac{2}{3} Y\right) \text{ sign } (S_1) \qquad (2.16)$$

The material strength dependence on P_0, Y_0, Y_m and P_m is summarized in Fig. 2.5. The shock loading path is also shown in the figure to have a slope of μ/k where k is the effective bulk modulus of the shock wave. This loading path is only valid for regions where the radial strain is much greater than the tangential strain, i.e., at the shock front.

In Section V the material strength formulation will be modified to include brittle failure and an effective stress law.
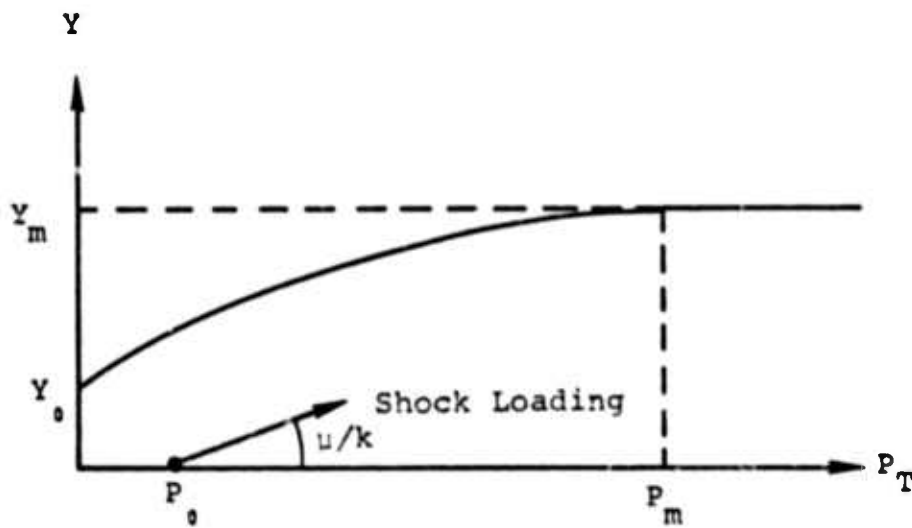
$$Y = \left(Y_0 + Y_m \frac{P_T}{P_m} \right) \left(2 - \frac{P_T}{P_m} \right) \qquad P_T < P_m$$

$$Y = Y_0 + Y_m \qquad\qquad\qquad\qquad P_T > P_m$$

Y_n = Maximum allowable stress difference

P_T = Hydrodynamic component of the stress tensor
including overburden pressure

P_0 = Overburden pressure

Figure 2.5. Assumed relationship between the material strength
(Y) and the hydrodynamic component of stress (P_T).

III. DISCUSSION OF RESULTS

3.1 THEORETICAL CONSIDERATIONS

A detailed discussion of the reduced displacement
potential, RDP, which serves as the equivalent elastic source
representation for spherically symmetric explosions is pre-
sented in Appendix A. The SKIPPER code, which is used to
propagate the shock wave into the elastic region is discussed
in Appendix B. The results presented in Fig. A.1 show the
calculated reduced velocity potential spectra using the
material model described in the preceding section. As noted
in Appendix A, the spectra are essentially flat in the tele-
seismic frequency band for device yields at least as large
as 200 kt. This result along with Eq. (A.9) imply that body
wave magnitude, m_b, has the proportionality

$$m_b \sim \log [c\Psi(\infty)] \qquad (3.1)$$

where $\Psi(\infty)$ is the steady state value of the RDP and c
is the near source compressional wave speed. Of course,
this relation does not include the effect of pP or any of
the details of the geophysical properties of the crustal
layers. It has been derived by considering the impedence
mixmatch between the low velocity source region and the
basement rock, i.e., a two layer earth model. It is pre-
fered to the homogeneous earth assumption which gives
$\Psi(\infty)/c$ for m_b proportionality.

If $\Psi_i(\infty)$ and $\Psi_k(\infty)$ are two values of $\Psi(\infty)$ corres-
ponding to materials i and k then the change in tele-
seismic magnitude is given by

$$\Delta m = m^i - m^k = \log \left[\frac{c_i \, \Psi_i(\infty)}{c_k \, \Psi_k(\infty)} \right] \qquad (3.2)$$

If material properties remain constant and the only change is the device yield, W, then cube root scaling gives

$$\Delta m = m^i - m^k = \log \frac{W_i}{W_k} \qquad (3.3)$$

Equation (3.2) gives the "scaling" law for teleseismic magnitudes in terms of $c\Psi(\infty)$. This equation is always valid as long as the spectrum of the equivalent source is flat within the teleseismic frequency band and path effects associated with earth structure are invariant between events.

It should be noted that uncertainties in yield estimates based on experimentally determined seismic magnitudes may be related to uncertainties in near source material properties via direct application of Eq. (3.2).

3.2   PARAMETER SENSITIVITY

The results of the sensitivity study are summarized in Table 3.1. Some general remarks are in order before discussing the effect of individual parameter variations. Note that the ambient density, ρ_0, and the bulk modulus, k_0, are included in the table although they are not independent parameters in the context of this study; i.e., their values are determined by the independent parameters appearing in the first ten columns. Calculation No. 18 is selected as the reference for body and surface wave magnitude variations in order to avoid the appearance of minus signs in the Δm_b column. Calculations marked with an asterisk in the $\Psi(\infty)$ column were performed with a new source description which gave an RDP 42 percent higher than the RDP obtained in Calculation No. 8 using the old source description; the RDP's calculated with the new source description were therefore scaled down by a factor of 0.704 and the scaled values are reported in Table 3.1. All calculations appearing in Table 3.1 were performed with a device yield of 20 tons.

TABLE 3.1

RESULTS OF PARAMETER SENSITIVITY STUDY

ξ_w	Φ_0	P_e (kbar)	P_c (kbar)	C (km/sec)	μ (kbar)	Y_0 (kbar)	Y_{MAX} (kbar)	P_m (kbar)	P_0 (kbar)	ρ_0 (gm/cm³)	k_0 (kbar)	$\Psi(\infty)$ (m²)	$\Delta\rho_b$	Calculation Number
0	0	—	—	3.81	40.0	0	0.5	0.6	0.116	2.4	294.4	13.88	1.2862	1
0.05	0	—	—	2.80	40.0	0	0.5	0.6	0.116	2.243	121.8	10.01	1.0104	2
0.136	0	—	—	2.44	40.0	0	0.5	0.6	0.116	2.015	66.5	7.85	0.8451	3
0.17	0	—	—	2.40	40.0	0	0.5	0.6	0.116	1.938	57.8	7.34	0.8088	4
0.19	0	—	—	2.38	40.0	0	0.5	0.6	0.116	1.895	53.8	7.09	0.7901	5
0.17	0.02	0.075	0.5	2.40	40.0	0	0.5	0.6	0.116	1.90	56.1	3.60	0.4994	6
0.17	0.05	0.075	0.5	2.40	40.0	0	0.5	0.6	0.116	1.84	52.6	2.10	0.2653	7
0.17	0.05	0.075	0.5	2.40	40.0	0	1.0	0.6	0.116	1.84	55.6	1.35	0.0734	8
0.17	0.05	0.15	0.5	2.40	40.0	0	1.0	0.6	0.116	1.84	52.6	1.48*	0.1133	9
0.17	0.02	0.075	0.5	2.40	40.0	0	0.5	0.6	0.075	1.90	55.1	4.20	0.5563	10
0.17	0.02	0.075	1.25	2.40	40.0	0	0.5	0.6	0.075	1.90	56.1	4.60	0.6059	11
0.17	0.05	0.075	0.5	2.32	40.0	0	1.0	0.6	0.116	1.84	45.7	1.31*	0.0456	12
0.17	0.05	0.075	0.5	2.25	40.0	0	1.0	0.6	0.116	1.84	39.8	1.29*	0.0257	13
0.17	0.05	0.075	0.5	2.40	42.0	0	1.0	0.6	0.116	1.84	50.0	1.28*	0.0503	14
0.17	0.05	0.075	0.5	2.40	45.0	0.1	1.0	0.6	0.116	1.84	46.0	1.17*	0.0113	15
0.17	0.05	0.075	0.5	2.40	40.0	0.2	1.0	0.6	0.116	1.84	52.6	1.32*	0.0637	16
0.17	0.05	0.075	0.5	2.40	40.0	1.0	1.0	0.6	0.116	1.84	52.6	1.31*	0.0604	17
0.17	0.05	0.075	0.5	2.40	40.0	0	1.0	1.25	0.116	1.84	52.6	1.14*	0	18
0.17	0.02	0.075	0.5	2.40	40.0	0	0.5	0.6	0.075	1.90	56.1	7.70	0.8296	19
0.17	0.02	0.075	0.5	2.40	40.0	0	0.5	0.6	0.348	1.90	56.1	2.41	0.3251	20
0.17	0.02	0.075	0.5	2.40	40.0	0	0.5	0.6	0.619	1.90	56.1	2.08	0.2612	21
0.17	0.05	0.075	0.5		40.0	0	0.75	0.6	0.116	1.84	52.6	1.51*	0.1221	22

*Calculation performed with new source description.

The effects of water content on seismic coupling are revealed by Calculations 1 through 5. The reduced displacement potential was calculated for five fully saturated tuffs having different mass fractions of water, f_w. Fully saturated tuffs were chosen in order to eliminate the effects of air-filled porosity. Note that adding water decreases both the density, ρ_0, and the bulk modulus of the mixture, k_0. Since the shear modulus is held constant at 40 kbars, variations in compressional wave speed, c, reflect only the changes in density and bulk modulus. Variations in body wave magnitude as functions of water mass fraction are described in Fig. 3.1. The decrease in seismic coupling as the water content is increased is to be expected. Since water is more compressible than rock at all pressures of interest, the amount of energy dissipated in the form of heat via shock loading increases with increasing water content, leaving less energy available for conversion into seismic radiation. m_b decreases by about 0.5 magnitude units as the mass fraction of water increases from 0 to 0.19.

The effect of air-filled voids on seismic magnitude is obtained from Calculations 4, 6 and 7. The water content is held constant at $f_w = 0.17$ for these and the remaining calculations in Table 3.1. The variation of seismic magnitude as a function of the void fraction, ϕ_0, is presented in Fig. 3.2. Note that the introduction of air-filled voids causes a drastic reduction in seismic coupling and the importance of establishing this parameter preshot is obvious.

Calculations 8 and 9 show that seismic magnitude is not sensitive to P_e, the pressure below which pore closure is elastic and fully recoverable. A factor of two increase in P_e increases the seismic magnitude by 0.04 units. Similarly, Calculations 10 and 11 show that magnitude is insensitive to variations in P_c, the pressure at which all ambient porosity is irreversible removed. An increase in P_c by a factor of
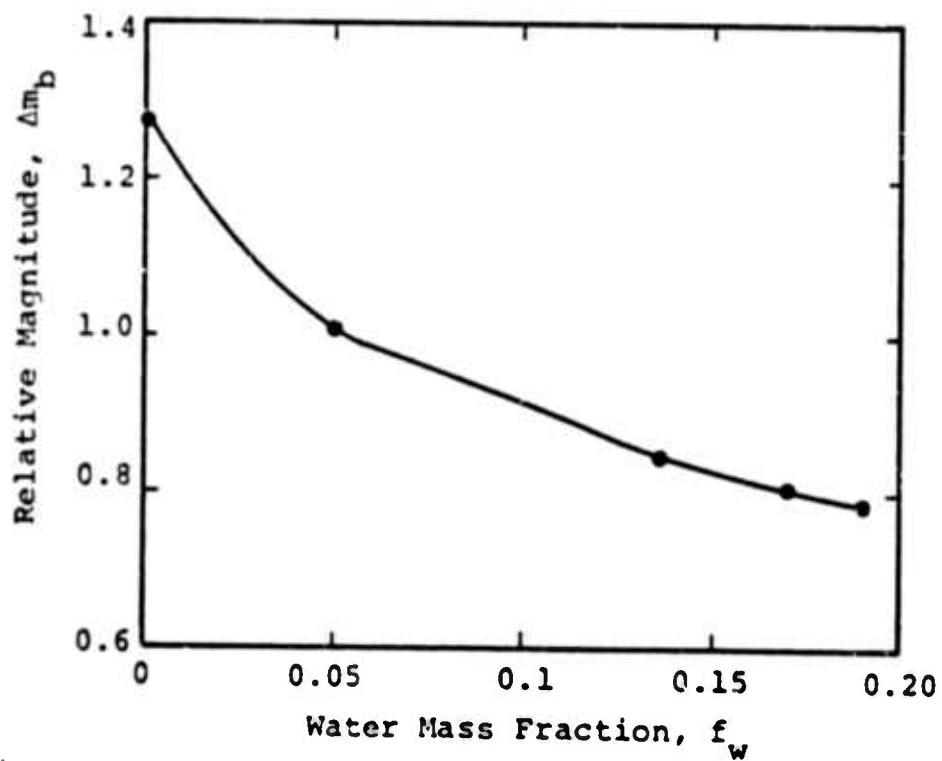
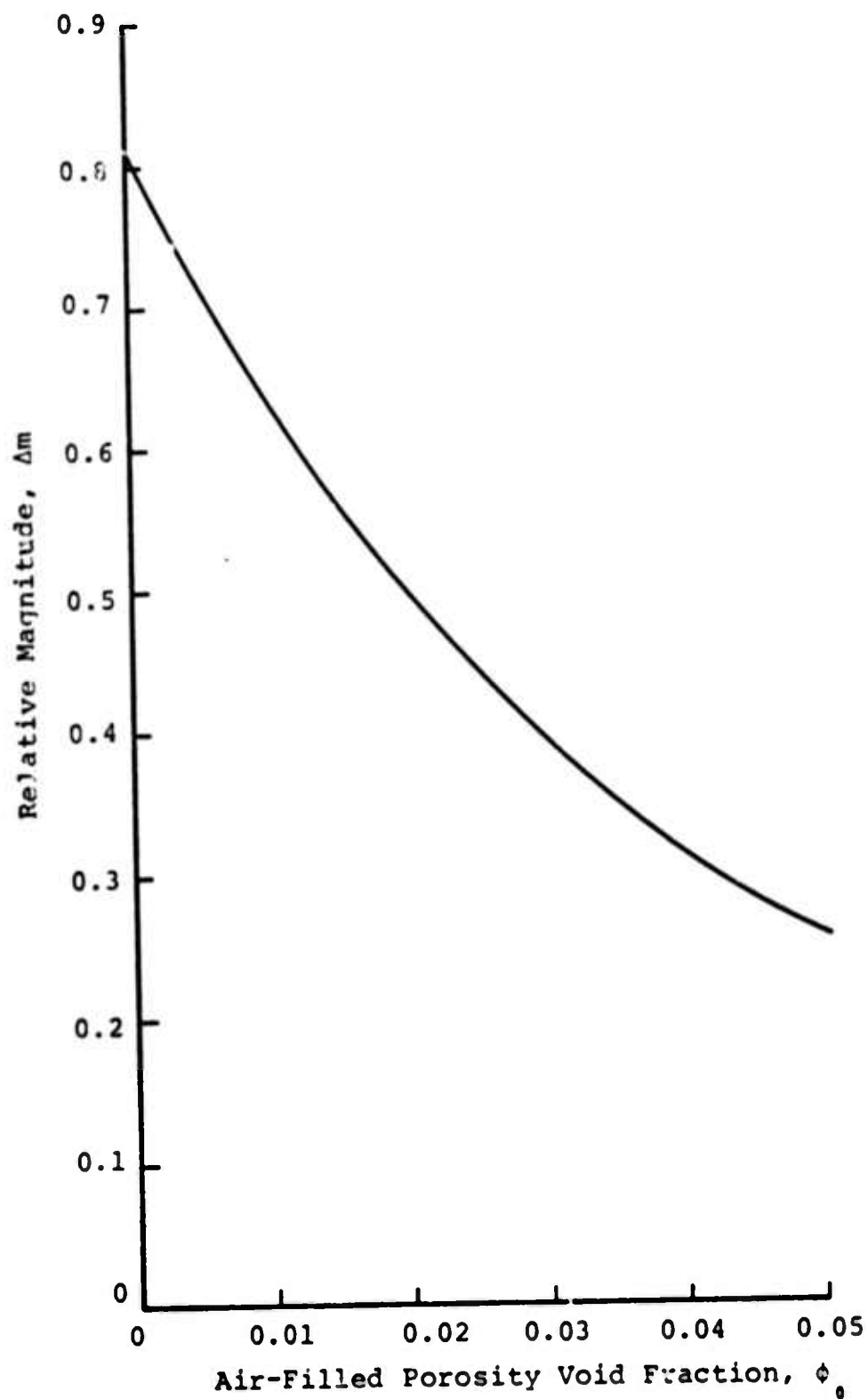Figure 3.1.   Variation of seismic magnitudes with water mass fraction.

Figure 3.2. Effect of air-filled porosity on seismic magnitude.

2.5 produces an increase in magnitude of 0.03 units. It should be noted that P_e and P_c are associated with the porosity model and might increase in importance as ϕ_0, the air-filled void fraction, is increased.

The effect of variations in near source seismic velocity, c, on magnitude is obtained from Calculations 8, 12 and 13. The permissible range of c is limited at this point because the properties of tuff, the properties of water, the mass fraction of water and the shear modulus are held constant. Variations in c therefore reflect only a change in the initial slope of the crush curve associated with the porosity model. As shown in F⁴   3, a 6 percent error in P wave velocity produces a cha. m_b of about 0.05 magnitude units. Increasing the compressional wave speed increases seismic coupling for body waves.

Calculations 8, 14 and 15 illustrate the effect of variations in the shear modulus on seismic magnitude. Body wave magnitude is reduced as the shear modulus increases as shown in Fig. 3.4.

The yield surface is described by the parameters Y_0, Y_m, and P_m. Calculations 8, 16, 17 and 18 show the effect of Y_0, the zero pressure yield strength, on seismic coupling. The variation of Δm with Y_0 is plotted in Fig. 3.5. Increases in Y_0 tend to reduce seismic coupling. The results of Calculations 7, 8 and 22 are plotted in Fig. 3.6 which shows the effect of Y_{MAX}, the maximum allowable material strength, on seismic magnitude. Increasing Y_{MAX} by a factor of two causes magnitude to decrease by 0.192 magnitude units, indicating that Y_{MAX} is a fairly sensitive parameter. For a given value of Y_{MAX}, the shape of the material strength surface is controlled by P_m, the pressure at which Y_{MAX} is attained. From Calculations 10 and 19 we see that increasing P_m by a factor of 2.08 causes magnitude to increase by 0.26 units. This result indicates that the shape of the failure surface plays an important role in determining
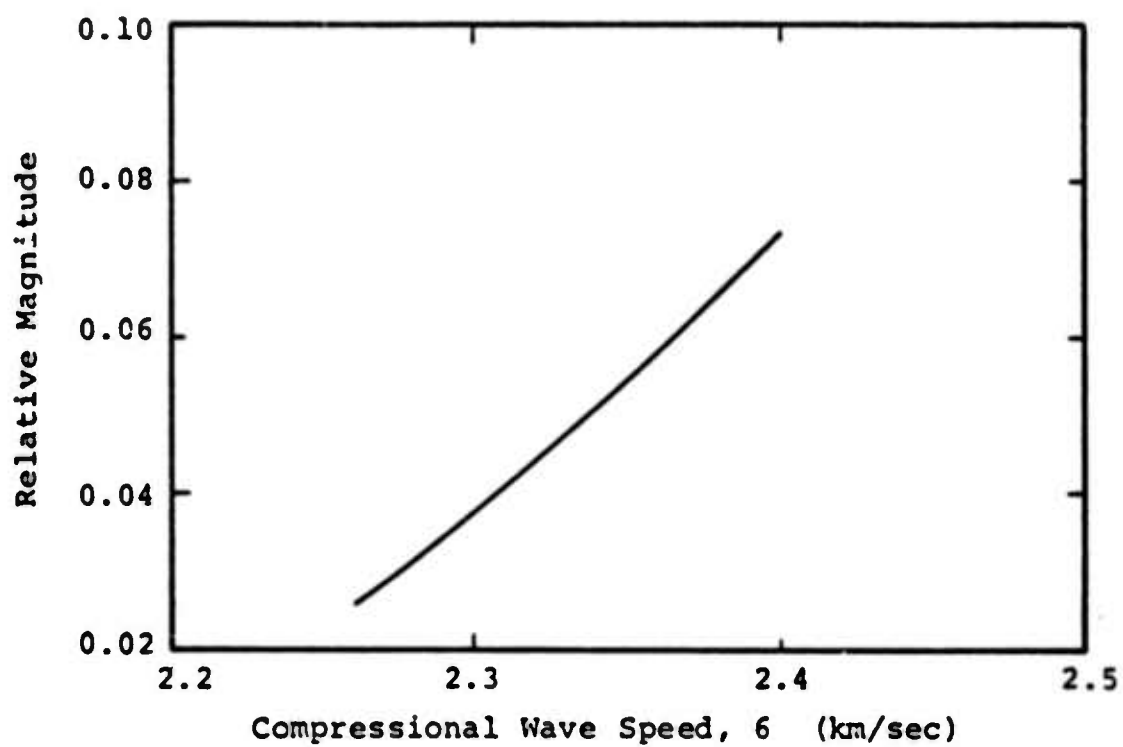
22

R-2742

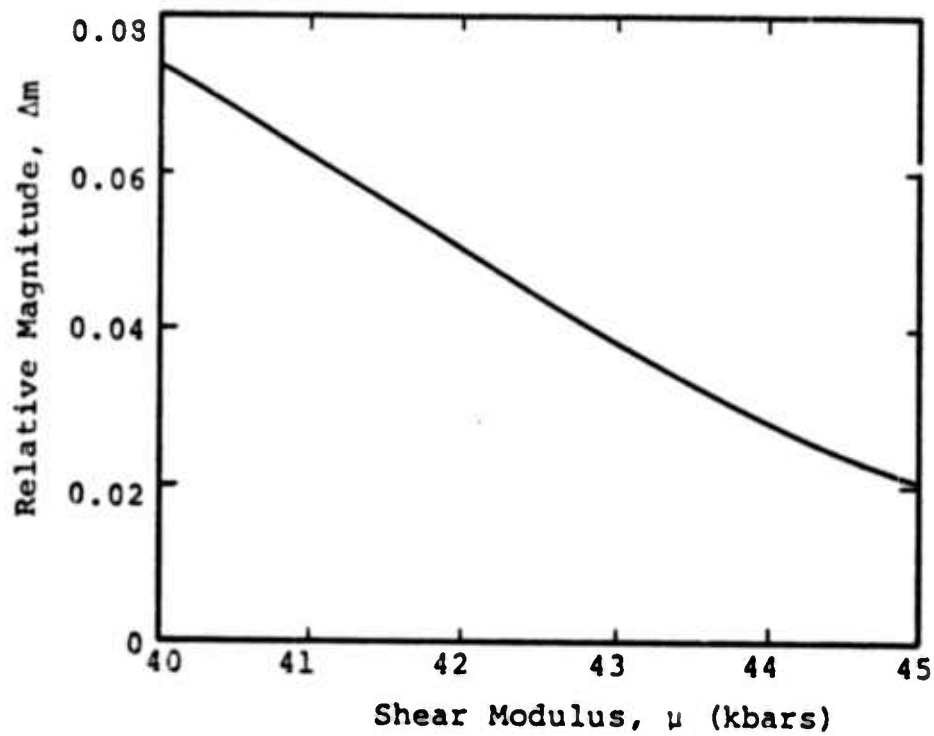Figure 3.3. Effect of compressional wave speed on seismic magnitude.

23

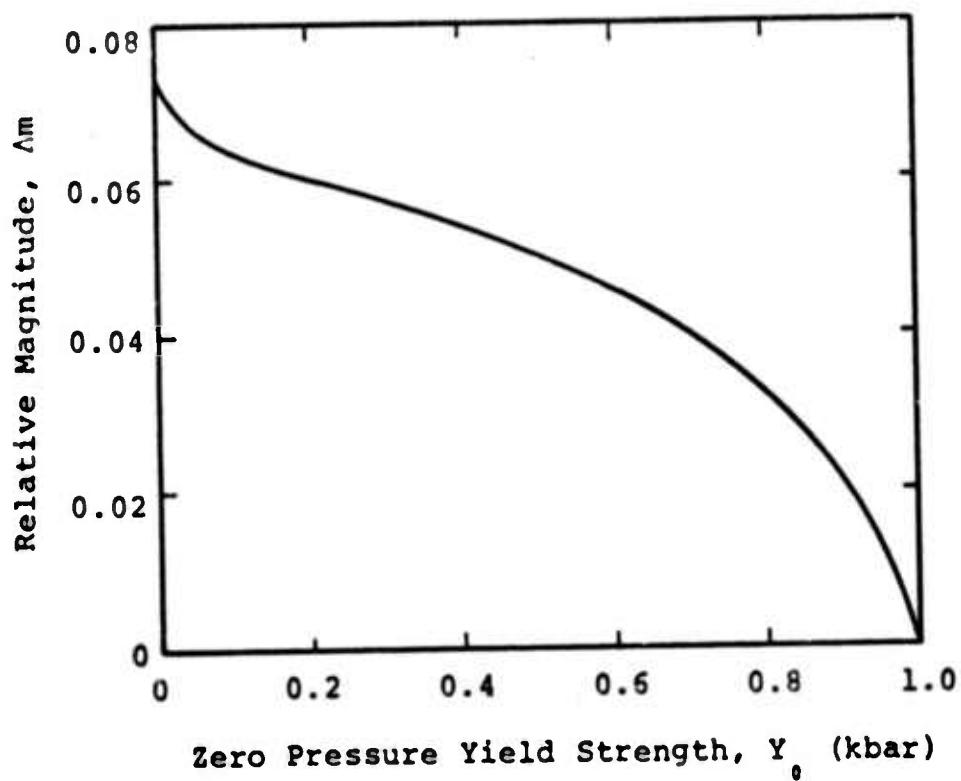Figure 3.4.   Effect of shear modulus on seismic magnitude.

Figure 3.5.   Effect of zero pressure yield strength on seismic coupling.
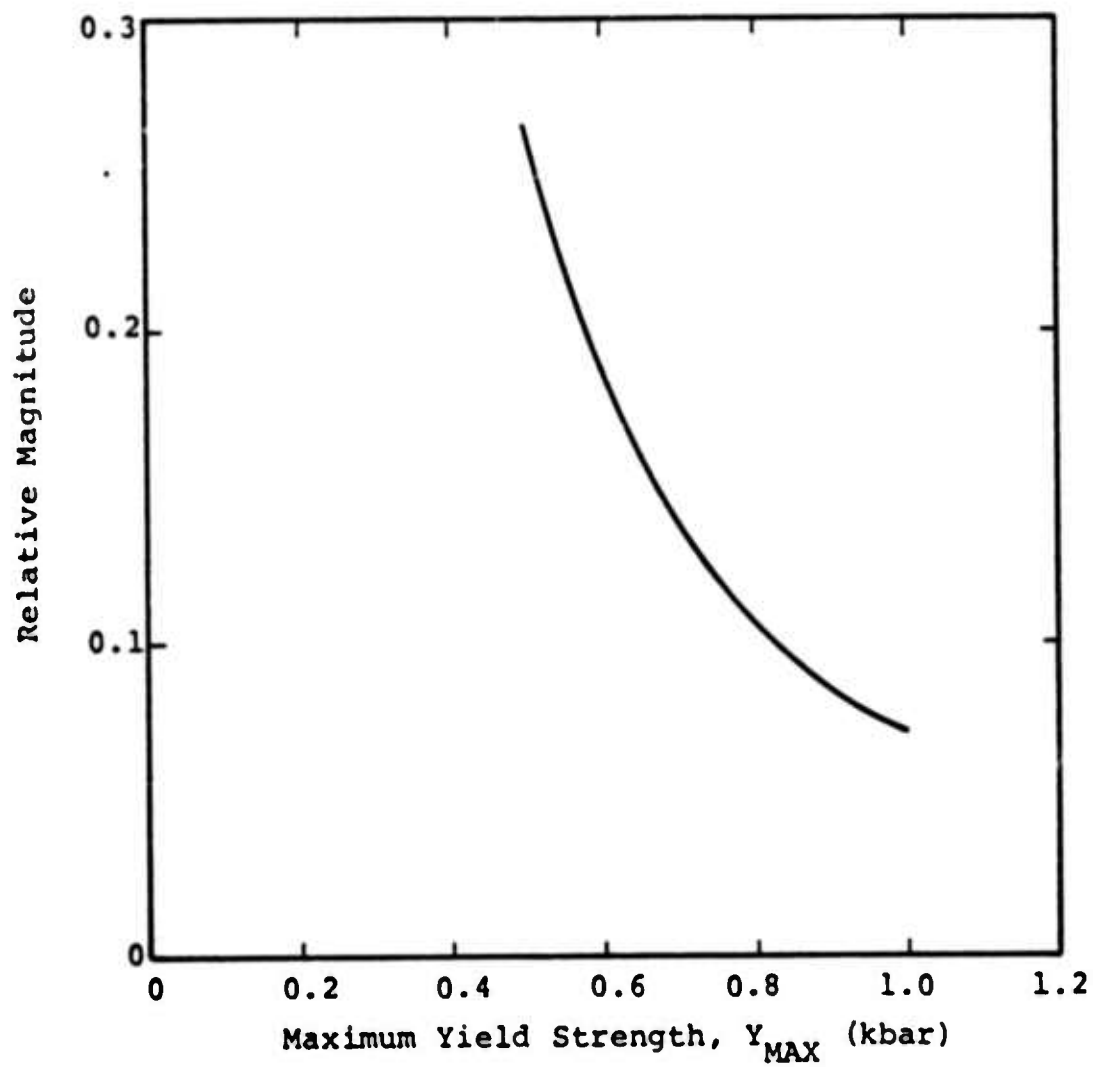
Figure 3.6. Effect of maximum material strength on seismic magnitude.

coupling efficiency. The material has less strength at low pressures when P_m is increased and we should expect a corresponding increase in magnitude. In fact, if any of the parameters Y_o, Y_m, or P_m are varied such that the material strength is enhanced, a decrease in coupling efficiency is observed.

The effect of overburden pressure, P_o, on magnitude, as determined by Calculations 6, 10, 20 and 21, is shown in Fig. 3.7. If all material properties are held constant, coupling efficiency decreases with increasing overburden pressure. An increase in the depth of burial, DOB, by a factor of six causes magnitude to decrease by a factor of two. The decrease in magnitude is not uniform with depth. An increase in DOB at shallow depths causes magnitude to decrease more than that caused by an equivalent increase in DOB at greater depths. This effect results from the rapid increase in material strength at low pressures. We should note that it is unlikely that material properties would remain invariant as overburden pressure is increased from 100 bars to 600 bars. An increased DOB usually corresponds to an increase in water content, resulting in decreased air-filled porosity and material strength.
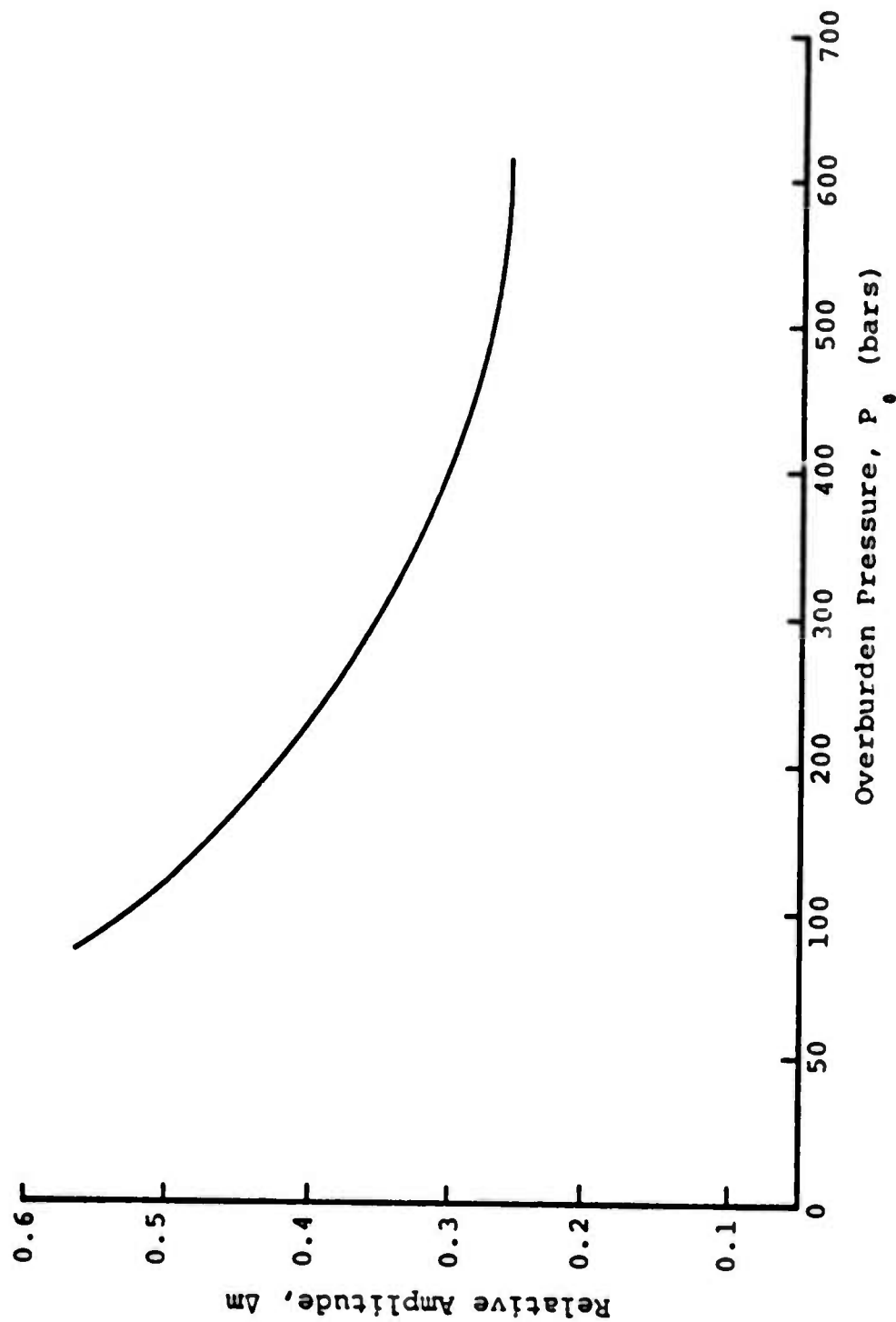
Figure 3.7. Effect of overburden pressure on seismic magnitude.

IV. SUMMARY OF RESULTS

The results of the parameter study provide valuable in-
sight concerning the importance of various material parameters
with respect to accurate prediction of seismic coupling. It
has been shown that increasing the overburden pressure, or,
equivalently, the depth of burial, decreases coupling effi-
ciency substantially. Therefore, the DOB must be accurately
known in order to make a reliable prediction of seismic magni-
tude. It is also desirable to know the properties of the
material in the immediate vicinity of the device; if sub-
stantial spatial variation of the material properties occurs
near the device or if the DOB is quite shallow it may be
necessary to consider two-dimensional effects which are not
treated here. Accurate prediction of seismic magnitudes
via one-dimensional spherically symmetric calculations is
therefore understood to be dependent on the material uni-
formity about the device.

Since the elastic properties of the near source mate-
rial appear in the magnitude relation, Eq. (3.2), via the P
wave velocity, c, it is obviously important to determine
their values accurately. A positive error in determination
of c would cause body wave magnitude to be over-predicted.
A positive error in μ would cause magnitude to be under-
predicted.

The steady state value of the RDP, $\Psi(\infty)$, which appears
in the magnitude relation, Eq. (3.2), is dependent on the
shock response of the near source material. The near source
material properties which have the most pronounced effect
on the shock response are the water mass fraction, f_w, and
the air-filled void fraction, ϕ_0. Positive errors in either
f_w or ϕ_0 could lead to substantial under-prediction of
seismic magnitudes. Seismic magnitude is not very sensitive

29

to P_e, the elastic pressure, and P_c, the crush pressure, indicating that details in the porosity model are relatively unimportant.

Seismic magnitudes are, however, very sensitive to the parameters which describe the failure surface. If Y_0, Y_m, or P_m are varied such that the material strength is enhanced the coupling efficiency of an explosive device is impaired. Thus, a positive error in the material strength would lead one to an under-prediction seismic magnitude.

V. THE EFFECT OF MATERIAL STRENGTH ON THE PRESSURE AND DEVIATORIC COMPONENTS OF THE STRESS TENSOR

5.1   INTRODUCTION

Most code calculations of the type presented in Section 3, either for ground shock predictions or equivalent source calculations, have assumed that material strength depends only on the pressure component of the stress tensor (i.e., Eq. (2.14)). Also, very little attention has been paid to the consequences of exceeding the allowable material strength other than envoking either an associated or non-associated flow rule, i.e., Eq. (2.16). Further, the influence of water content on material strength via an effective stress law has not been considered in any ground shock calculation performed to date.

A number of investigators have considered the above topics separately. In particular, Cherry and Petersen[7] have identified the dependence of material strength on the third deviatoric invariant. Maenchen and Sack[10] presented a formulation for tension failure which is ideally suited for a stress wave code. Garg and Nur[11] investigated the consequences of various effective stress laws on the interpretation of experimental data. We have relied heavily on the results of these investigators in order to formulate the strength portion of the constitutive model.

5.2   THE DEPENDENCE OF MATERIAL STRENGTH ON THE STRESS INVARIANTS

Figure 5.1 is taken from Cherry and Petersen[7] and shows the improvement in the definition of material strength, Y, when P is replaced by $\overline{P}$. Similar improvement has also been found for granite, limestone and glass. Y, P and $\overline{P}$ are obtained from the stress invariants J_1, J_2', J_3', as follows:
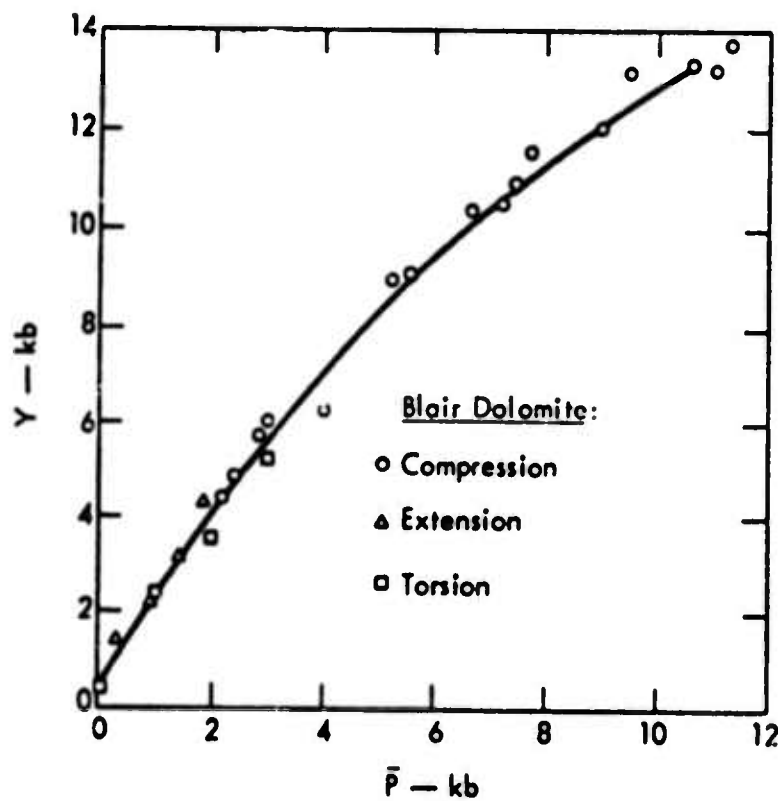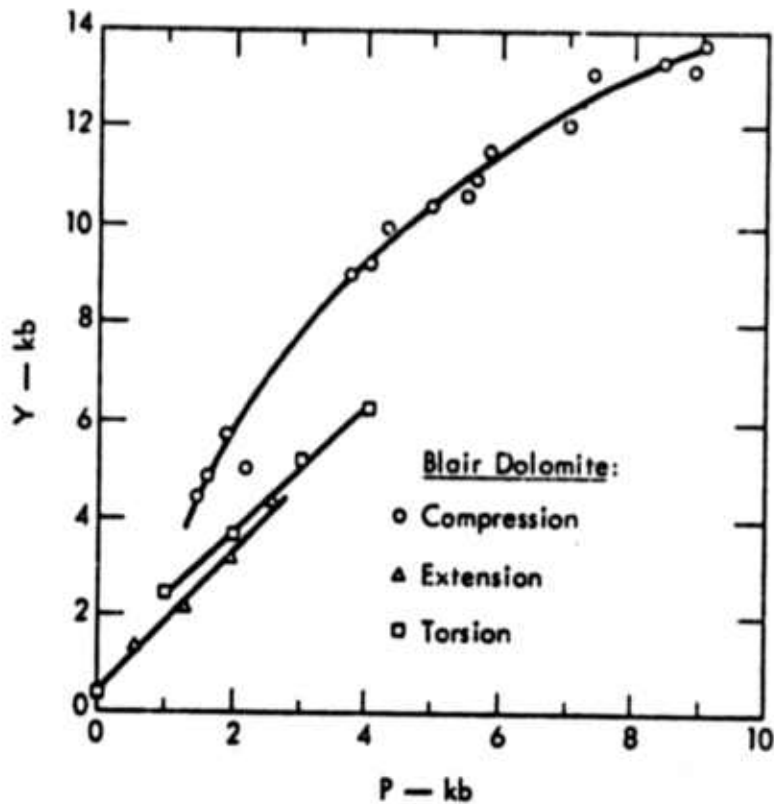
Figure 5.1. These figures are from Cherry and Petersen [1970] and show the improvement in failure surface definition when P is replaced by P̄. The strength data are from Handin, et al. [1967].

$$Y = (3J_2)^{1/2} \tag{5.1}$$

$$\bar{P} = P - \frac{1}{2}\left(\frac{J_3'}{2}\right)^{1/2} \tag{5.2}$$

$$P = -\frac{J_1}{3} \tag{5.3}$$

P is now the pressure component of the stress tensor discussed in Section II with the overburden pressure, P_0, added. J_1, J_2' and J_3' are the first, second deviatoric and third deviatoric stress invariants. If σ_{11}, σ_{22}, σ_{33} are principal stresses, then

$$J_1 = \sigma_{11} + \sigma_{22} + \sigma_{33} \tag{5.4}$$

$$J_2' = \frac{(\sigma_{11}+P)^2 + (\sigma_{22}+P)^2 + (\sigma_{33}+P)^2}{2} \tag{5.5}$$

$$J_3' = (\sigma_{11}+P)(\sigma_{22}+P)(\sigma_{33}+P) \tag{5.6}$$

Note that when the intermediate principal stress, σ_{22}, is equal to either the maximum, σ_{11}, or minimum, σ_{33}, principal stress, then

$$Y = |\sigma_{11} - \sigma_{22}| \tag{5.7}$$

$$\bar{P} = -\left(\frac{\sigma_{11} + \sigma_{22}}{2}\right) \tag{5.8}$$

The functional form we have chosen to represent the variation of material strength, Y, with the stress state, $\bar{P}$, is identical to that used in Section 2, i.e.,

$$Y = \left\{ Y_0 + \frac{Y_m}{\overline{P}_m} \ \overline{P} \left[2 - \frac{\overline{P}}{\overline{P}_m} \right] \right\} \left[1 - \frac{e}{e_m} \right] \quad \begin{matrix} \overline{P} < \overline{P}_m \\ \\ e < e_m \end{matrix}$$

$$Y = (Y_0 + Y_m) \left[1 - \frac{e}{e_m} \right] \quad \begin{matrix} \overline{P} > \overline{P}_m \\ \\ e < e_m \end{matrix} \qquad (5.9)$$

$$Y = 0 \qquad\qquad e > e_m$$

where Y_0, Y_m, $\overline{P}_m$ and e_m are input constants. These constants along with P_0, the overburden pressure, determine the variation of material strength with stress state along with the initial stress state, P_0, corresponding to the overburden pressure at the depth of burial of the device.

The material strength dependence on P_0, Y_0, Y_m and $\overline{P}_m$ is summarized in Fig. 5.2. The shock loading path is also shown in the figure to have a slope of $1-2\sigma$, where σ is Poisson's ratio. This loading path is only valid for regions where the radial strain is much greater than the tangential strain, i.e., at the shock front.

5.3   SHEAR FAILURE

Hooke's law is used to obtain an initial estimate of the stress deviators, i.e.,

$$\hat{S}_{ij}^{n+1} = S_{ij}^{n} + 2\mu \ \dot{e}_{ij} \ \Delta t \qquad (5.10)$$

where $\hat{S}_{ij}^{n+1}$ and S_{ij}^{n} are the values of the stress deviator at time $t + \Delta t$ and t respectively.

μ is the shear modulus

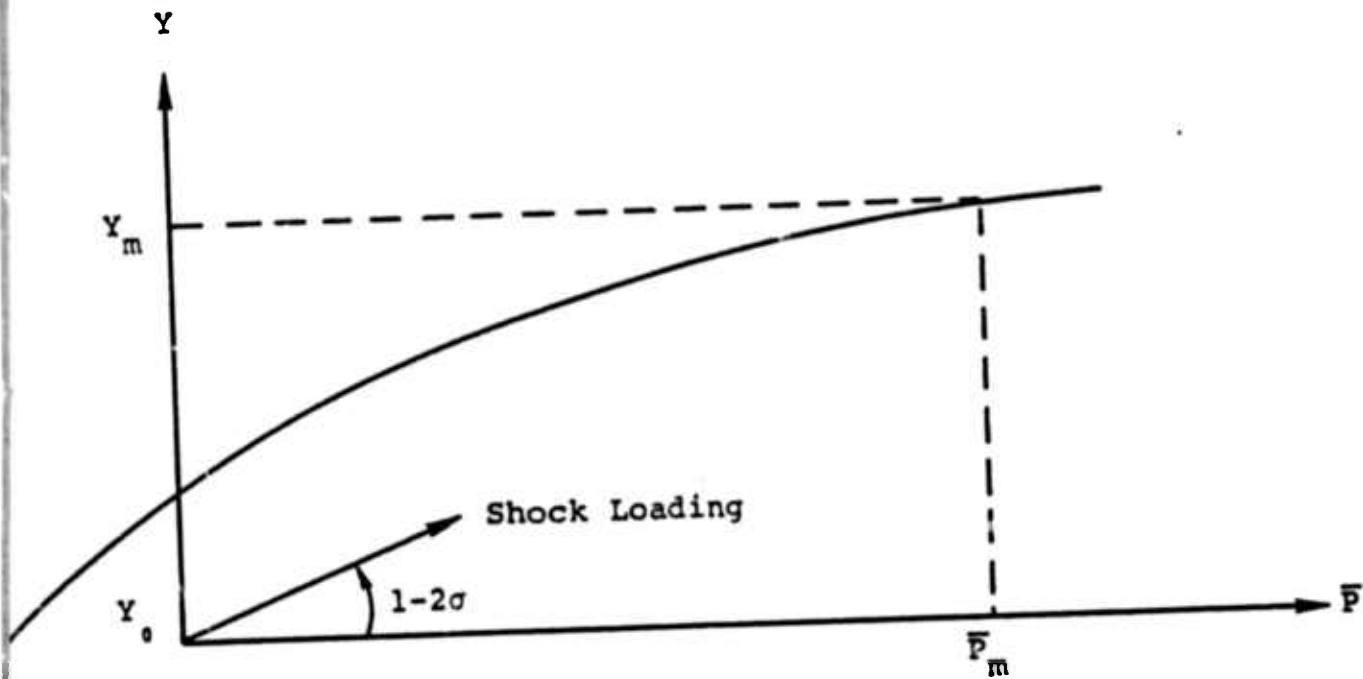$\dot{e}_{ij}$ is the strain rate devaitor

Δt is the time increment

Figure 5.2. Dependence of Y on Y , $\overline{P}_m$ and Y_m. When $\overline{P}$ is used for the abcissa. The shock loading path has a slope of $1-2\sigma$.

Shear failure occurs if the material strength, given by Eq. (5.9) and evaluated at $\hat{\bar{P}}$, is exceeded, i.e., if

$$J > Y(\hat{\bar{P}}) \tag{5.11}$$

where

$$J = \left[\frac{3}{2} \left(\hat{S}_{11}^{2} + \hat{S}_{22}^{2} + \hat{S}_{33}^{3} \right) \right]^{1/2} \tag{5.12}$$

$$\hat{\bar{P}} = P^{n+1} - \frac{1}{2} \left(\frac{\hat{S}_{11} \hat{S}_{22} \hat{S}_{33}}{2} \right)^{1/3} \tag{5.13}$$

P^{n+1} includes the overburden pressure and we have omitted the n+1 superscript on $\hat{S}_{ij}$.

If $J > Y(\bar{P})$ then adjustment of the stress deviators, $\hat{S}_{ij}^{n+1}$, is required. We assume that

$$S_{ij}^{n+1} = a \, \hat{S}_{ij}^{n+1} \tag{5.14}$$

where S_{ij}^{n+1} is the adjusted value of the stress deviator and

$$a = \frac{Y(\hat{\bar{P}}) + \frac{b}{2} \left(\frac{\hat{S}_{1} \hat{S}_{2} \hat{S}_{3}}{2} \right)^{1/3}}{J + \frac{b}{2} \left(\frac{\hat{S}_{1} \hat{S}_{2} \hat{S}_{3}}{2} \right)^{1/3}} \tag{5.15}$$

$$b = \frac{dY}{d\bar{P}} \quad \text{(evaluated at } \hat{\bar{P}}\text{)} \tag{5.16}$$

Equation (5.15) is obtained by approximating the strength function at $\hat{\bar{P}}$ with a first order Taylor series and assuming that no adjustment in P^{n+1} occurs during shear failure.

36

5.4   TENSION FAILURE

Tension failure is assumed to occur in the element if
a principal stress is greater than zero and if the inequality
of (5.11) has ever been satisfied. We then apply the tension
failure model proposed by Maenchen and Sack[10] and introduce
an inelastic strain normal to the crack. This inelastic strain
is just sufficient to zero the tensile stress.

For example, if $\hat{\sigma}_{11}$, $\hat{\sigma}_{22}$ and $\hat{\sigma}_{33}$ are the three princi-
pal stresses and if $\hat{\sigma}_{11}$ is greater than zero, then the ad-
justed stress $(\sigma_{11}, \sigma_{22}, \sigma_{33})$ are given by

$$\sigma_{11} = \hat{\sigma}_{11} - (k + \frac{4}{3}\mu)\, \Delta e_{11}$$

$$\sigma_{22} = \hat{\sigma}_{22} - (k - \frac{2}{3}\mu)\, \Delta e_{11} \qquad (5.17)$$

$$\sigma_{33} = \hat{\sigma}_{33} - (k - \frac{2}{3}\mu)\, \Delta e_{11}$$

where

$$\Delta e_{11} = \frac{\hat{\sigma}_{11}}{k + \frac{4}{3}\mu} \qquad (5.18)$$

k is the bulk modulus, μ is the shear modulus and all
stresses include the overburden pressure.

If two of the principal stresses, say σ_{11} and σ_{22}
are greater than zero, then the stress adjustment becomes

$$\sigma_{11} = \hat{\sigma}_{11} - (k - \frac{2}{3}\mu)(\Delta e_{11} + \Delta e_{22}) - 2\mu\Delta e_{11}$$

$$\sigma_{22} = \hat{\sigma}_{22} - (k - \frac{2}{3}\mu)(\Delta e_{11} + \Delta e_{22}) - 2\mu\Delta e_{22} \qquad (5.19)$$

$$\sigma_{33} = \hat{\sigma}_{33} - (k - \frac{2}{3}\mu)(\Delta e_{11} + \Delta e_{22})$$

where

$$\Delta e_{11} = \frac{(k + \frac{4}{3}) \hat{\sigma}_{11} - (k - \frac{2}{3} \mu) \hat{\sigma}_{22}}{4\mu (k + \frac{\mu}{3})}$$

(5.20)

$$\Delta e_{22} = \frac{(k + \frac{4}{3} \mu) \hat{\sigma}_{22} - (k - \frac{2}{3} \mu) \hat{\sigma}_{11}}{4\mu (k + \frac{\mu}{3})}$$

All the inelastic strain increments $(\Delta e_{11}, \Delta e_{22}, \Delta e_{33})$ are accumulated on each cycle giving

$$E_{11}^{n+1} = E_{11}^{n} + \Delta e_{11}$$

$$E_{22}^{n+1} = E_{22}^{n} + \Delta e_{22}$$

(5.21)

$$E_{33}^{n+1} = E_{33}^{n} + \Delta e_{33}$$

These equations give the basic stress-strain adjustment during tension failure. However, they apply equally well for crack closure. If at least one of the total strains in Eq. (5.21) (say E_{11}^{n}) is greater than zero, then the crack will open or close depending on the sign of $\hat{\sigma}_{11}$. If $\hat{\sigma}_{11} > 0$, then

$$\Delta e_{11} > 0$$

$$E_{11}^{n+1} > E_{11}^{n}$$

and the crack width increases. The inequalities are reserved if $\hat{T}_{11} < 0$ and the crack width decreases. Closure will continue until

$$E_{11}^{n} + \Delta e_{11} < 0 .$$

38

Then

$$\Delta e_{11} = - E^n_{11}$$

$$E^{n+1}_{11} = 0$$

and the crack is completely closed. When this state is achieved the element is able to support a compressive stress in the (1,0,0) direction.

5.5   EFFECTIVE STRESS

All effective stress laws, formulated for fluid-saturated porous rocks, assume that the fluid pressure should be included in the calculation of the stress state which determines material strength. An excellent review of various definitions of effective stress and their consequences in terms of laboratory strength data has been given by Garg and Nur.[11]

The definition of stress state we have adopted is $\bar{P}$, where $\bar{P}$ is given by Eq. (5.2). If P_p is the pore fluid pressure, then the effective stress state becomes

$$\bar{P} = P - \frac{1}{2}\left(\frac{J_2'}{2}\right)^{1/3} - F(P_p)$$

where $F(P_p)$ is a positive function of the pore fluid pressure. We have assumed that $F(P_p)$ behaves as follows:

$F(P_p) = 0$ if tension cracks are open. (5.22)

$F(P_p) = 0$ if P has never exceeded the crush pressure, P_c. (5.23)

$F(P_p) = 0$ if $P - \frac{1}{2}\left(\frac{J_2'}{2}\right)^{1/3} < 0$. (5.24)

If none of the above apply, then

$$F(P_p) = P - \frac{1}{2}\left(\frac{J_2'}{2}\right)^{1/3} .$$

(5.25)

The conditions given in Eqs. (5.22) and (5.23) assume that the pore fluid pressure has no effect on the stress state when air filled porosity exists in the element. If no air filled porosity exists, then Eqs. (5.24) and (5.25) apply.

Figure 5.3 shows the effect on material strength when $P > P_c$. The relaxation to Y_0 is achieved by assuming the material behaves like a Maxwell solid. The stress deviator S_{ij} is given by

$$S_{ij}^{n+1} = \hat{S}_{ij}^{n+1} \left[1 - \frac{\Delta t}{\delta} \left(1 - \frac{Y_0}{J} \right) \right] \qquad J > Y_0$$

$$S_{ij}^{n+1} = \hat{S}_{ij}^{n+1} \qquad\qquad J \leq Y_0$$

(5.26)

where $\hat{S}_{ij}^{n+1}$ and J are determined using Eqs. (5.10) and (5.12). The relaxation time, $\delta/(1-Y_0/J)$, increases as J approaches Y_0. This gives a smooth transition between the Maxwell solid and elastic behavior.

The behavior of $F(P_p)$ and the subsequent relaxation process given by Eqs. (5.22) through (5.26) is certainly an oversimplification of the role of pore fluid pressure in determining effective stress. Future work on this topic should merge experimental data of the type obtained by Duba, et al.[12] with the theoretical work of Garg and Nur.[11] We do feel, however, that the main features of effective stress are presently contained in the model. The primary input parameters which control the process are Y_0, P_c and δ. At least some insight concerning the appropriate values for Y_0 and P_c should be able to be obtained from laboratory experiments. The value assumed for δ controls the relaxation time and we have used close-in time history data to determine this parameter.
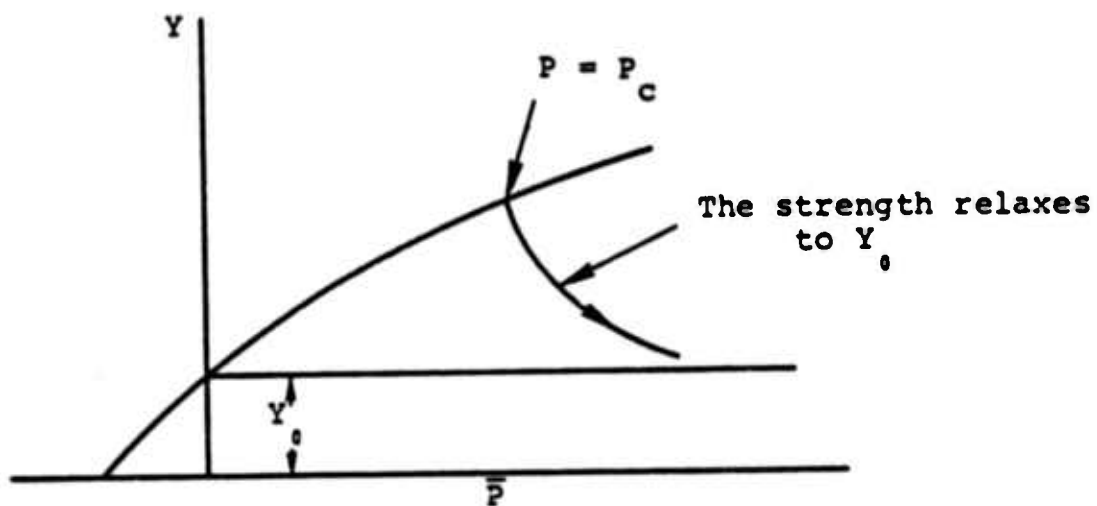
Figure 5.3.   The relaxation of material strength when all
              air filled porosity has been removed.

5.6 SUMMARY OF INPUT PARAMETERS FOR MATERIAL STRENGTH

The limiting value of material strength, $Y(\overline{P})$, is
obtained by specifying Y_0, Y_m, $\overline{P}_m$ and e_m. The function $Y(\overline{P})$
is given in Eq. (5.11). Except for the definition of $\overline{P}$,
these parameters and $Y(\overline{P})$ are identical to that of Section
2.2. The overburden pressure P_0 is required to determine
the ambient stress state of the material which is also re-
quired in Section 2.2. The crush pressure, P_c, plays a dual
role. First it determines the limiting pressure at which
the steepest release path occurs in the P-V plane, as shown
in Fig. 2.4. Second, it establishes the pressure at which
an effective stress law is used to determine material strength
as shown in Fig. 5.3. The parameter δ determines the re-
laxation time of the stress deviators during the application
of the effective stress law.

It is worth emphasizing that the only new parameter
introduced in this section is δ, the relaxation time. How-
ever, the interpretation of material failure has changed
considerably over the simple plastic flow model used in
Section 2, Eq. (2.16). We now present some of the conse-
quences of this revision.

5.7   THE CONSEQUENCES OF MATERIAL FAILURE ON THE EQUIVALENT
       ELASTIC SOURCE

A number of equivalent source calculations were per-
formed using the material strength constitutive model pre-
sented in Sections 5.2 through 5.5. Table 5.1 lists the key
material parameters used in the calculations along with the
calculated values of $\Psi(\infty)$ and the final cavity radius, R_{cav},
for a device yield of 0.02 kt.

The input data listed in Table 5.1 has been taken from
a number of sources. In particular the rock mechanics labora-
tory data of Stephens, Schock and Heard at the Lawrence Liver-
more Laboratory were used for granite and rhyolite. The data
taken by Terra Tek for many events at NTS Area 12 were used
for tuff. We should note, however, that no material strength
data could be found for saturated rhyolite. We assumed that
the material strength of this rock type would be the same
as granite.

Figures 5.4 and 5.5 show velocity time histories re-
corded at two distances from Piledriver, a 60 kt event in
granite at NTS (Parret[13]). In the past, most calculations
using measured granite strength data have been unsuccesful
in duplicating these velocity histories.

Figures 5.6 and 5.7 show the velocity histories ob-
tained from our calculation of the Piledriver event (Calcula-
tion 130) and Table 5.2 summarizes the comparison between the
calculation and the data. Cavity radius and peak velocities
at the two stations agree with the data to within 5 percent.
However, residual displacement at our first station is too
high. This is due largely to the difficulty in reproducing
the large negative phase of the velocity pulse of Fig. 5.4.
Since this difficulty has been encountered in all previous
calculations of Piledriver, it was decided to concentrate
on the second station. Here we attained excellent agreement
with the velocity data, including the long duration negative
phase of the pulse. This gave us good agreement with the
residual displacement measurement as well.

TABLE 5.1

REPRESENTATIVE MATERIAL PROPERTIES DATA FOR VARIOUS TEST AREAS

Name	ρ gm/cm³	C km/sec	μ kbars	Y_m kbars	Y_o kbars	$\bar{P}_m$ kbars	P_o bars	ϕ_o	P_c kbars	P_e bars	f	$\psi(\infty)$ m'	R_{cav} m
Piledriver													
130	2.67	5.33	207	7.7	0.3	9.0	80	0	1.0	0	0	9.23	3.2
Pahute Mesa Saturated Rhyolite													
124	2.45	4.2	169	7.7	0.3	9.0	200	0	0.5	0	4.0	7.2	3.4
125									1.0			4.2	2.8
Area 12 Tuff													
127	1.91	2.4	40	0.35	0.05	2.0	56	1.6	0.5	20	17.0	14.5	6.1
Hoggar Granite													
129	2.67	5.33	207	7.7	0.3	9.0	80	—	0	0	0	1.6	1.9
128												1.37	1.9

Calculation 128 used the same material properties as 129 except no tension failure was permitted in 128.

TABLE 5.2

COMPARISON BETWEEN DATA AND CALCULATION
FOR PILEDRIVER

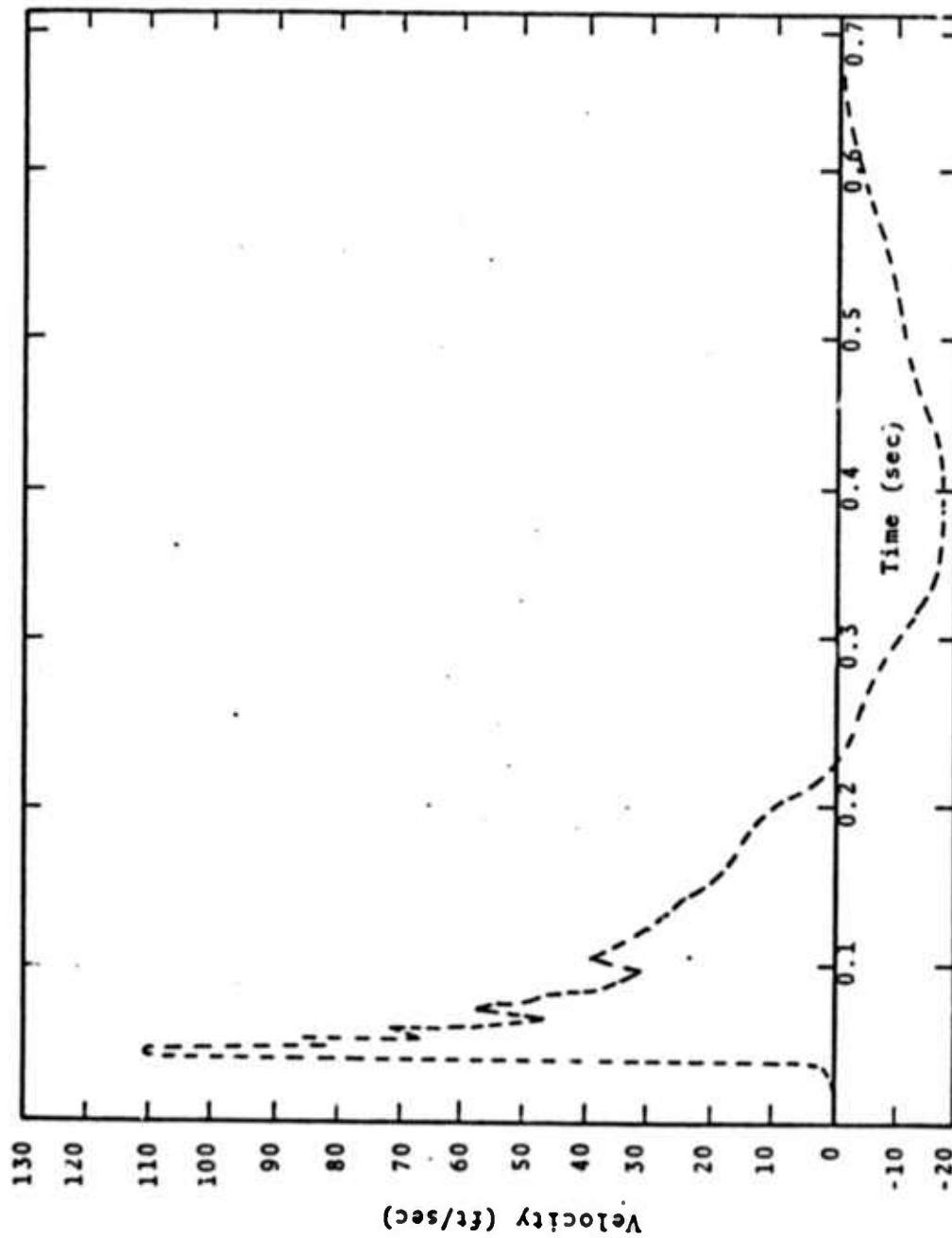|	Data	Calculation
Cavity radius (meters)	44.5	46.5
Peak Velocity ft/sec		
Station 1 (660' range)	110	103
Station 2 (1543' range)	18.8	19.4
Residual displacement (inches)		
Station 1	22	38
Station 2	7.2	6.1

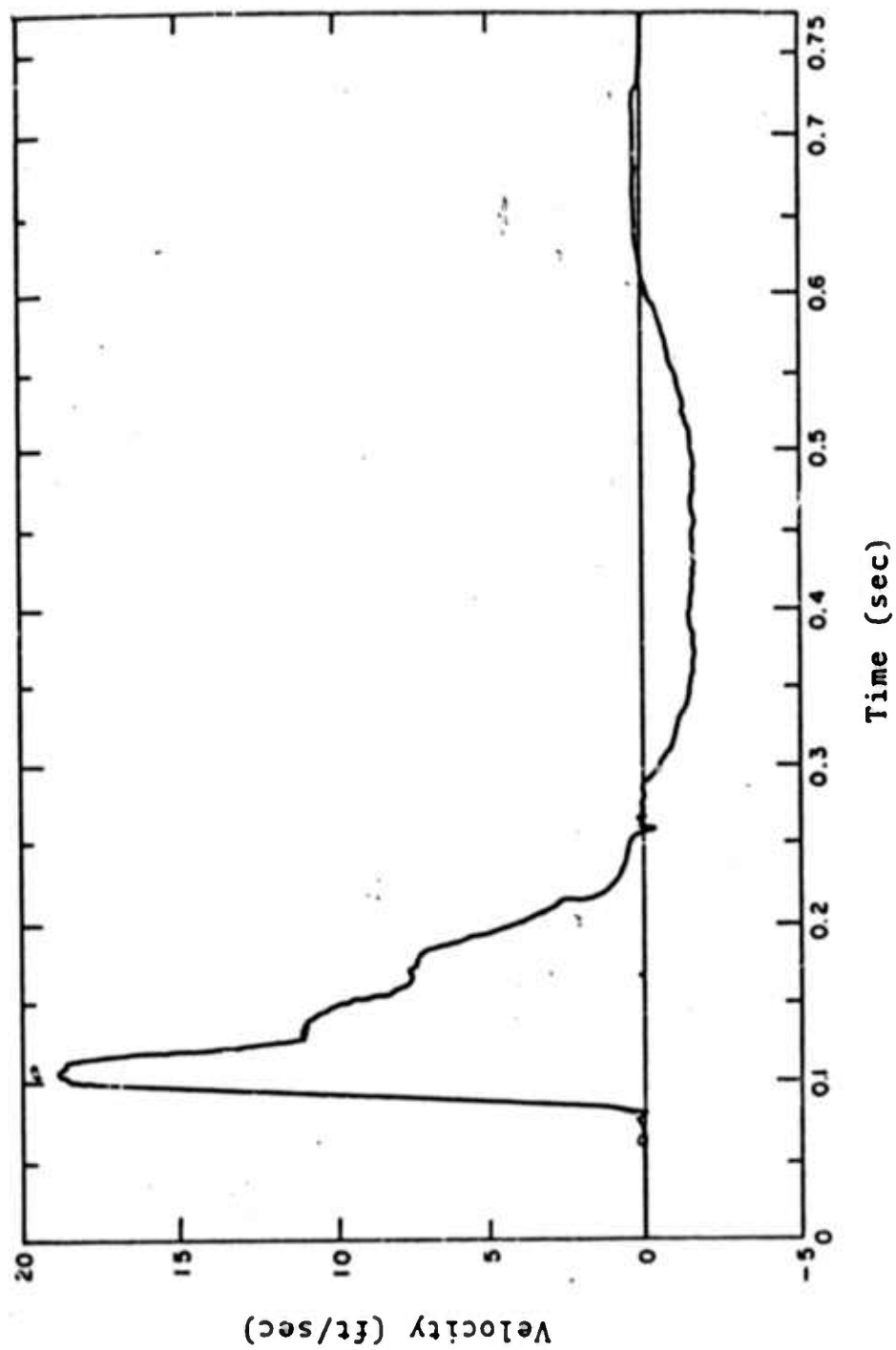Figure 5.4. Velocity history at 668 feet horizontal range from Piledriver. [13]
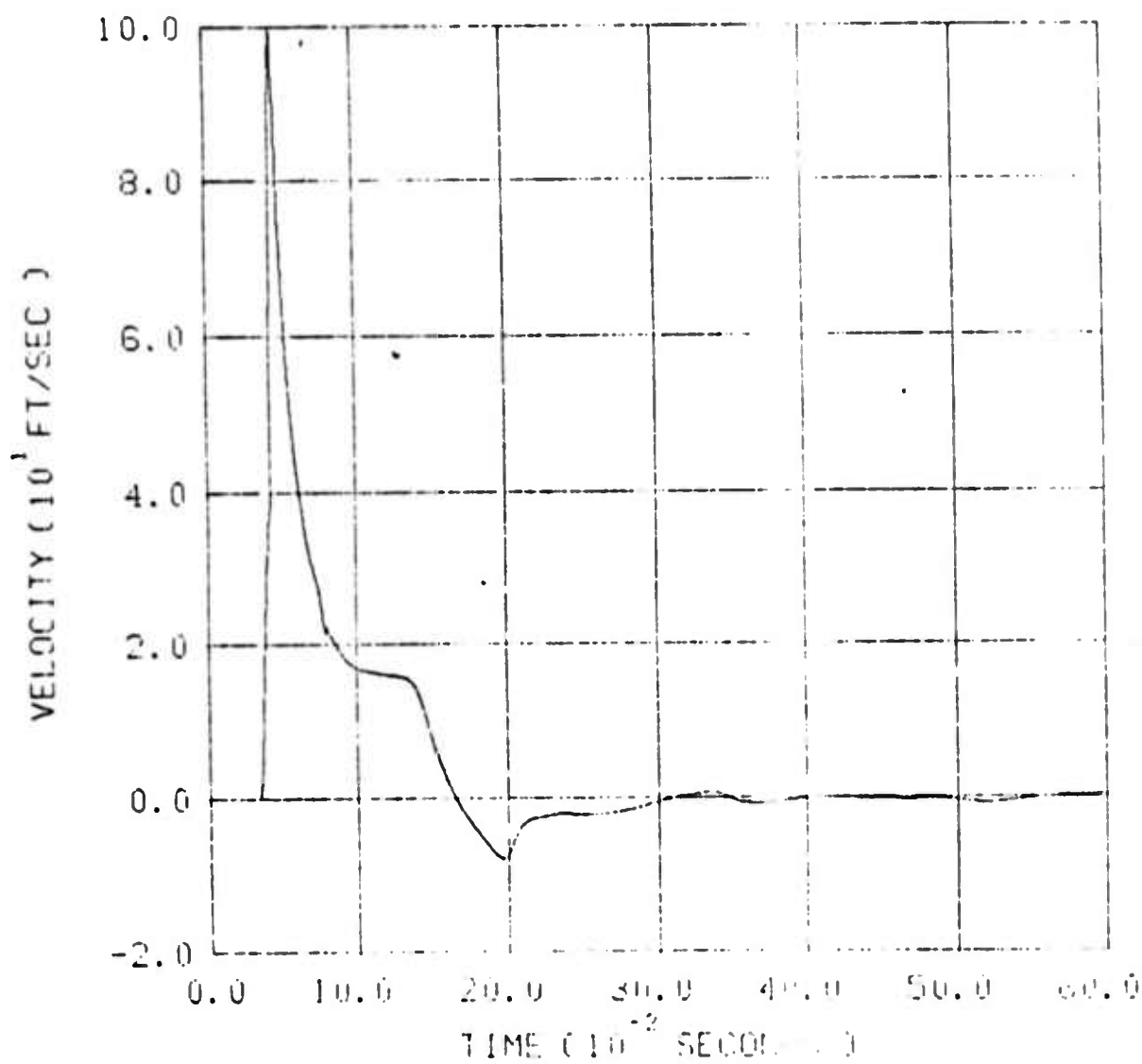
Figure 5.5.   Velocity history at 1543 feet horizontal range from Piledirver. [13]

Figure 5.6. Calculated particle velocity at 668 feet from
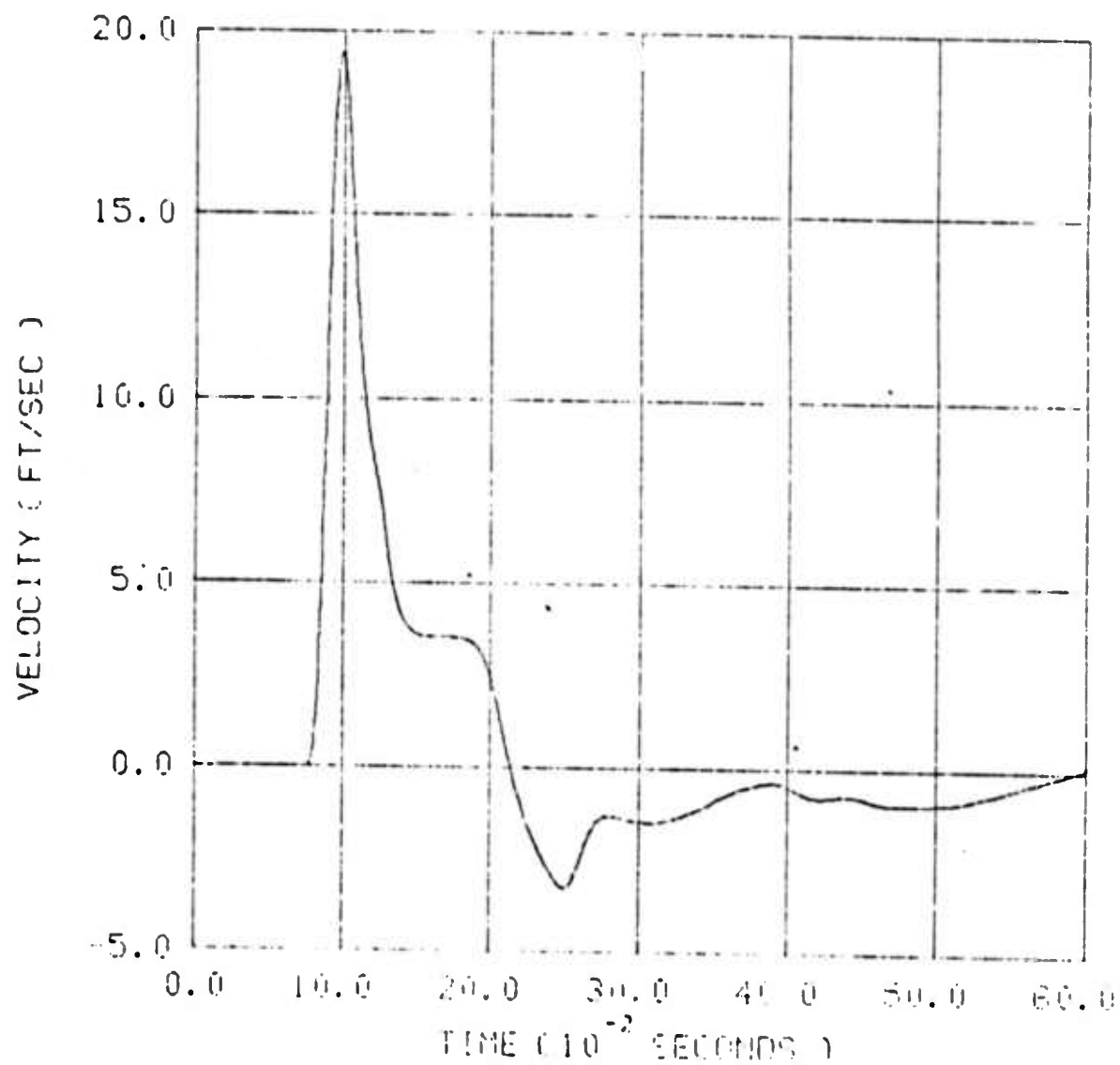Piledriver.

Figure 5.7. Calculated particle velocity at 1548 feet
from Piledriver.

The Hoggar Granite calculation was intended to be representative of the source coupling for the French nuclear tests conducted in the Sahara. For this environment P_c was assumed infinite, a value which corresponds to a dry material. From Table 5.1 we find that the calculated cavity radius for Piledriver was 3.2 meters while for the Hoggar granite the cavity radius was 1.9 meters. This gives a factor of five difference in cavity volumes between the two test areas which is consistent with the published French test results.

Figure 5.8 shows the source functions corresponding to Calculations 127, 130 and 125. Both the Piledriver and Pahute Mesa spectra are noticeably peaked. The amplitude of the peak seems to correlate directly with Y_0.

In order to identify the physical phenomenon responsible for the peak we show the two Hoggar source spectra corresponding to Calculations 128 and 129 in Figs. 5.9 and 5.10. For Calculation 128 neither stress relaxation or tension failure was allowed and the source spectrum is flat; a result which is identical to the spectra shown in Fig. A.2 in Appendix A. Tension failure was permitted in Calculation 129 and the spectral peak for this calculation is approximately a factor of three greater than $\Psi(\infty)$.

The effect of stress relaxation on spectral shape is obtained by comparing the source spectra from Calculations 124 and 125. The total relaxation is less for 124 than for 125 since the corresponding values of P_c are 0.5 kbar and 1.0 kbar. Figure 5.11 compares the source spectra from these two calculations and indicates that the greater the stress relaxation the larger the spectral peak when compared to $\Psi(\infty)$.

Both tension failure and stress relaxation within the inelastic region seem to be the primary physical mechanisms responsible for producing a peaked spectrum. There is a good explanation for this since both mechanisms introduce a
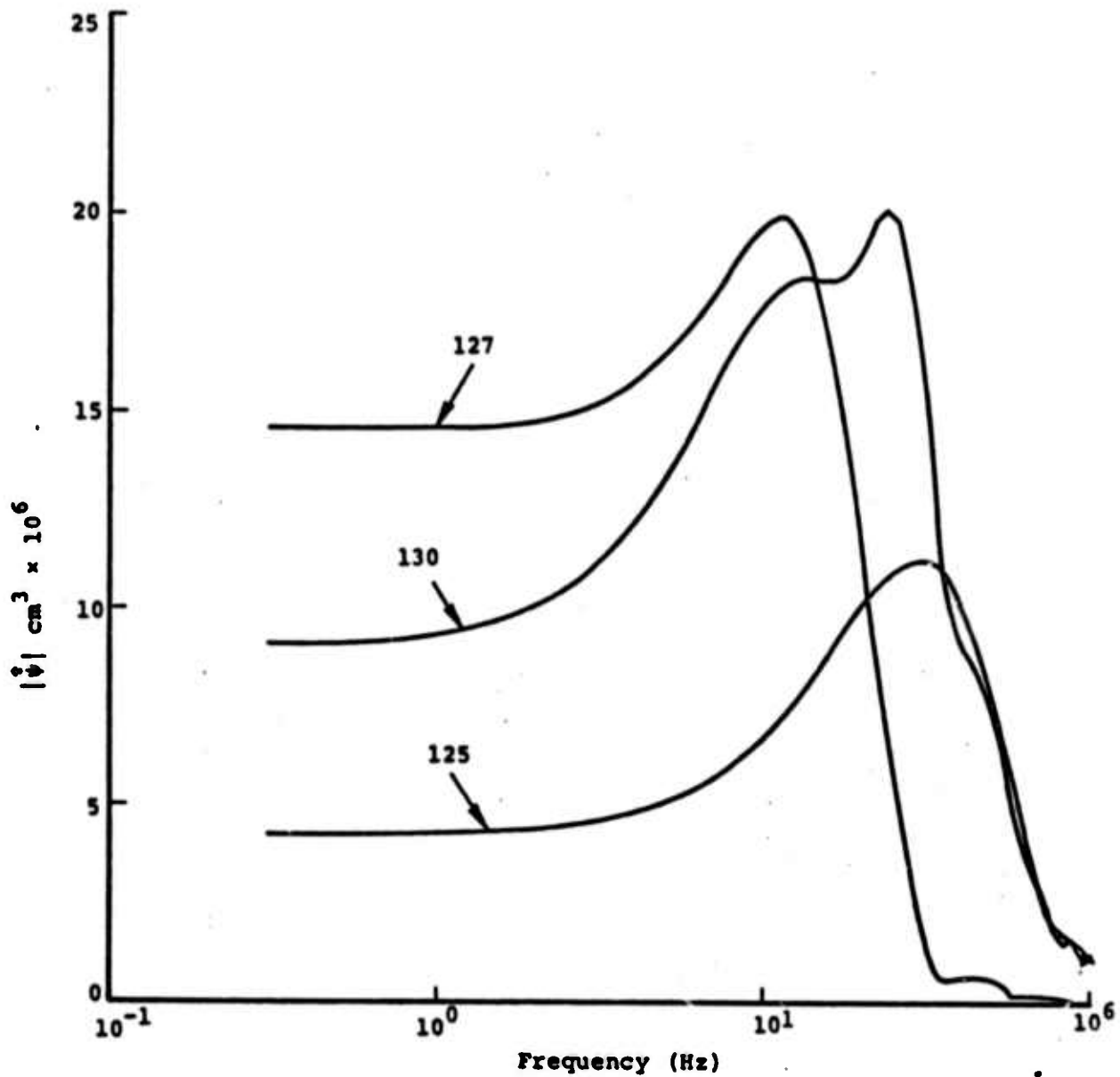
Figure 5.8. Equivalent source functions for Calculations 125, 127 and 130.
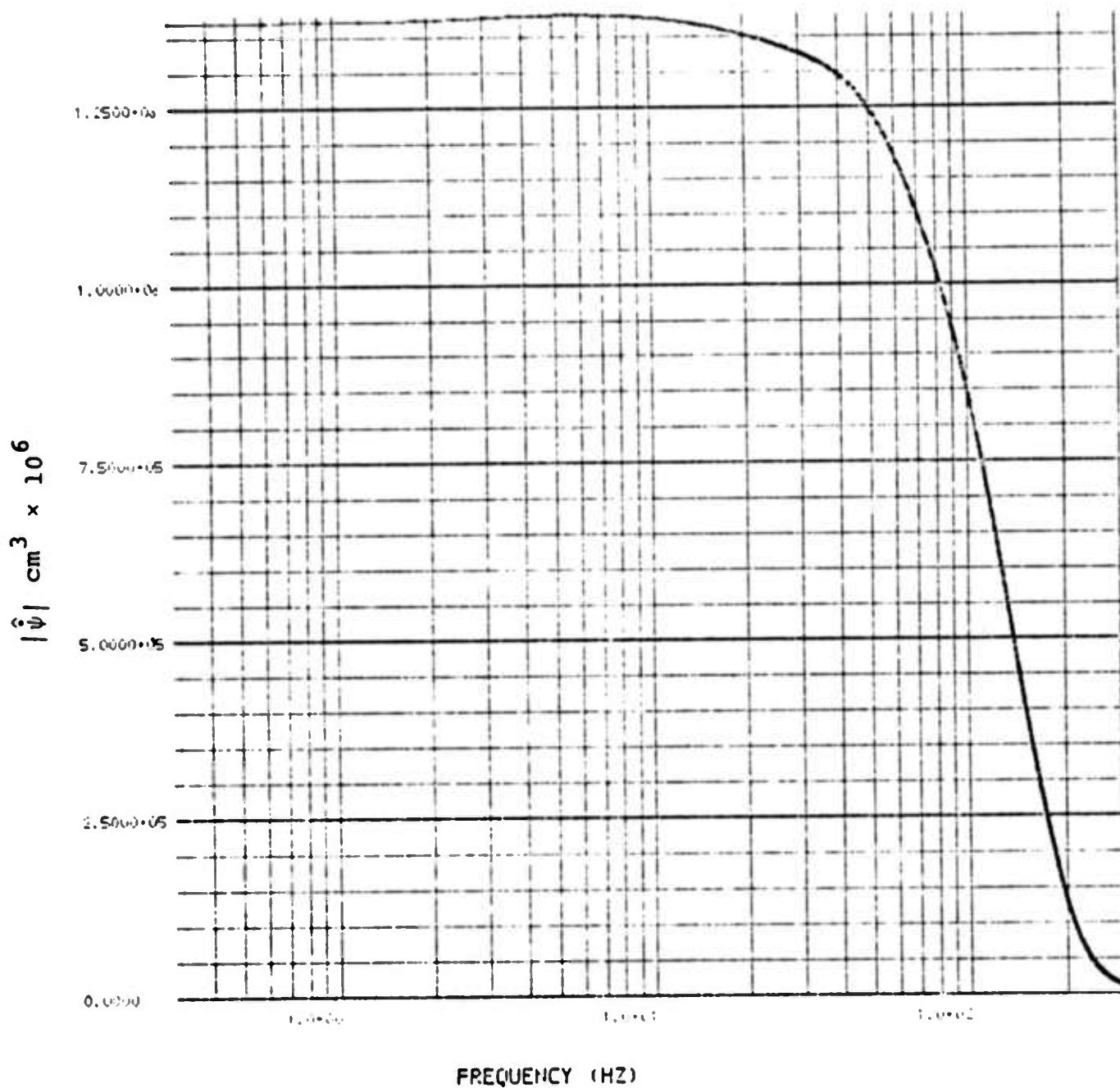
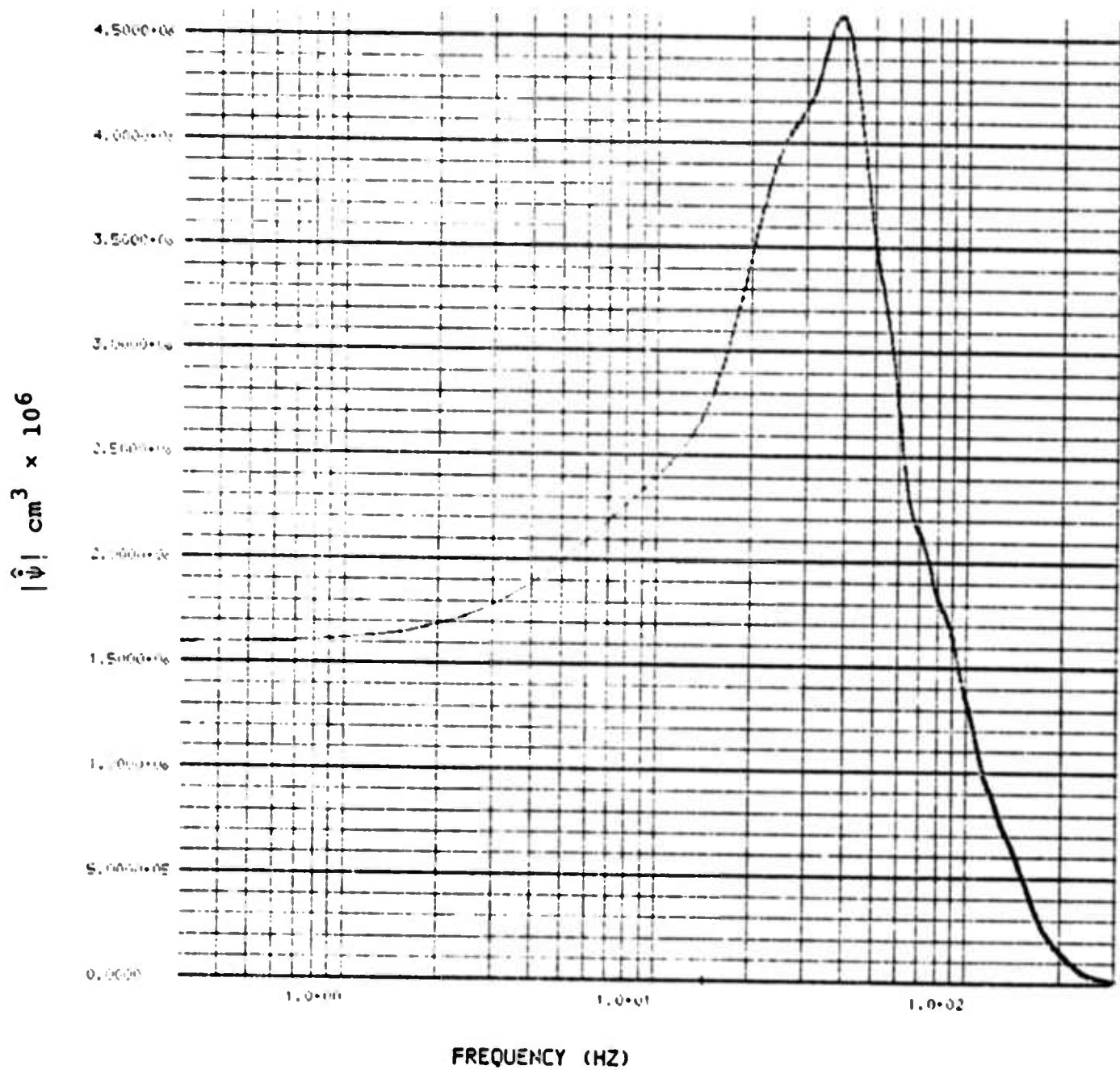Figure 5.9.   Equivalent source function for Calculation 128.

Figure 5.10.   Equivalent source function for Calculation 129.

discontinuity in the magnitude of allowable stress between the nonlinear and linear elastic regions. This discontinuity causes the velocity field in the elastic region to rarefy, i.e., to become negative. The negative portion of the velocity time history, shown in Fig. 5.7, causes the peak in the source spectrum.
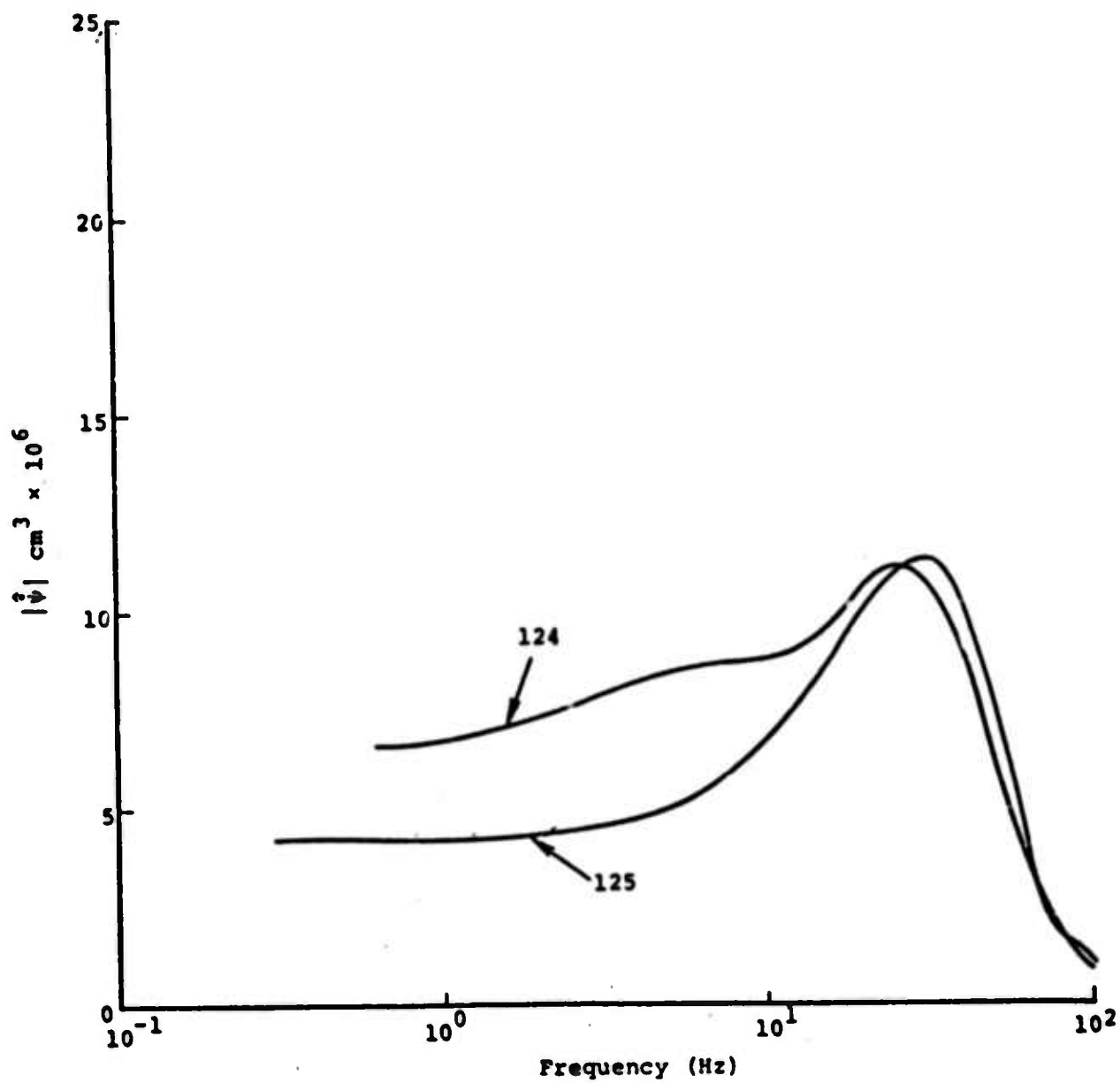
Figure 5.11.   Equivalent source spectra for Calculations
124 and 125.

REFERENCES

1. Bache, T. C., J. T. Cherry, K. G. Hamilton, J. F. Masso and J. M. Savino, "Application of Advanced Methods for Identification and Detection of Nuclear Explosions from the Asian Continent," Semi-Annual Technical Report, Systems, Science and Software, SSS-P-75-2646, May 1975.

2. Riney, T. D., J. K. Dienes, G. A. Frazier, S. K. Garg, J. W. Kirsch, D. H. Brownell, Jr., and A. J. Good, "Ground Motion Models and Computer Techniques," DNA 2195Z, 3SR-1071, 1972.

3. Herrman, W., "Constitutive Equation for the Dynamic Compaction of Ductile Porous Materials," J. Appl. Phys., 40, 1969.

4. Cherry, J. T., C. B. Archambeau, G. A. Frazier, A. J. Good, K. G. Hamilton, and D. J. Harkrider, "The Tele-seismic Radiation Field from Explosions: Dependence of Seismic Amplitudes upon Properties of Materials in the Source Region," Systems, Science and Software Formal Report, DNA 3113Z, 1973.

5. Stephens, D. R., H. C. Heard, and R. N. Schock, "High Pressure Mechanical Properties of Tuff from the Diamond Dust Site," Lawrence Livermore Laboratory Report UCRL-50858, April 27, 1970.

6. Cameron, I. G., and G. C. Georgie, "Dynamics of Intense Underground Explosions," J. Inst. Math. Applics., 4, 194-222, 1968.

7. Cherry, J. T. and F. L. Peterson, "Numerical Simulation of Stress Wave Propagation from Underground Nuclear Explosions," in Engineering with Nuclear Explosives, Vol. 1, 1970. Available from the Clearinghouse for Federal Scientific and Technical Information, National Bureau of Standards, Springfield, VA.

8. Wilkins, M. L., "Calculation of Elastic-Plastic Flow," Methods in Computational Physics, Vol. 3, Academic Press, 1964.

9. Blake, F. G., "Spherical Wave Propagation in Solid Media," J. Acoust. Soc. Am., 24, 2, 1952.

10. Maenchen, G. and S. Sack, "The TENSOR Code," in Methods in Computational Physics, Vol. 3, Academic Press, New York, 1964.

11. Garg, S. K. and A. Nur, "Effective Stress Laws for Fluid Saturated Porous Rocks," J.G.R., Vol. 78, No. 26, September 1973.

12. Duba, A. G., H. C. Heard and M. L. Santar, "Effect of Fluid Content on the Mechanical Properties of Westerly Granite,"Lawrence Livermore Laboratory, UCRL-51626, 1974.

13. Perret, W. R., "Free Field Ground Motions in Granite," Operation Flint Rock, Shot Piledriver, DASA POR-4001, 1968.

14. Bjork, R. L. and M. L. Gittings, "Wave Generation by Shallow Underwater Explosions," Systems, Science and Software Report 3SR-1008, DNA-2949Z, 1972.

15. Handin, J., H. C. Heard and J. N. Magouirk, "Effect of the Intermediate Principal Stress on the Failure of Limestone, Dolomite and Glass at Different Temperatures and Strain Rates," J.G.R., 72, 1967.

APPENDIX A

THEORETICAL SCALING OF m_b WITH REDUCED DISPLACEMENT POTENTIAL

The equivalent elastic source for a spherically symmetric explosion is often represented by a reduced displacement potential, $\Psi(\tau)$. This quantity completely characterizes the coupling of the explosion into elastic waves in the immediate source region. Therefore, we expect proportionality between Ψ and teleseismic waves. While this proportionality can be quite complicated, it is useful to have a simple scaling law which indicates the variation of teleseismic body wave amplitude with Ψ and the properties of the emplacement material. Such a scaling relationship is derived in this appendix.

We begin by reviewing the most elementary model, that of a delta function source in a one material or homogeneous earth model. We then add material inhomogeneity in the form of a second material and allow a more complex source representation, arriving at the scaling

$$|u_t| \approx \alpha_s \Psi_\infty^e \tag{A.1}$$

where $|u_t|$ is the amplitude of some consistently measured phase on the teleseismic record and Ψ_∞^e is a constant which characterizes the amplitude of the explosion generated pulse.

A Spherically Symmetric Source in a Homogeneous Earth

A spherically symmetric point source of dilatational waves can be characterized by a reduced displacement potential. That is, the radial displacement $u_s(R,t)$ can be written

$$u_s(R,t) = -\frac{\partial}{\partial R}\left(\frac{\Psi(\tau)}{R}\right) = \frac{\Psi(\tau)}{R^2} + \frac{\dot{\Psi}(\tau)}{R\alpha_s} \tag{A.2}$$

58

where $\tau = t - R/\alpha_s$, the time retarded by the P wave travel time to the position R. Here α_s is the P wave velocity in the source region.

Taking Fourier transforms, (A.2) may be written

$$\hat{u}_s(R,\omega) = \left(\frac{1}{R^2} + \frac{ik_\alpha}{R}\right) \hat{\Psi}(\omega) \, e^{-ik_\alpha R} \, , \tag{A.3}$$

where $k_\alpha \equiv \omega/\alpha_s$. If $k_\alpha R \gg 1$, that is, if R is many wavelengths, only the "far field" terms need to be retained and

$$\hat{u}_s(R,\omega) = \frac{\hat{\dot{\Psi}}(\omega)}{R\alpha_s} e^{-ik_\alpha R} \, . \tag{A.4}$$

For teleseismic body wave amplitudes only frequencies less than about 2.5 Hz are of importance. Then for low yield explosions $\hat{\dot{\Psi}}(\omega)$ is essentially constant and equal to Ψ_∞, the static value of the reduced displacement potential.* Therefore, for a low yield source of the type discussed in Section IV, and a homogeneous earth model, we have

$$|u_t| \approx \frac{\Psi_\infty}{\alpha_s} \tag{A.5}$$

For higher yields the teleseismic frequency band includes portions of the peak on the $\hat{\dot{\Psi}}(\omega)$ curves. Therefore Eq. (A.5) is improved by replacing Ψ_∞ by an "equivalent" value, Ψ_∞^e, which is yield dependent. Once again, this is

---
*The assumption that $\hat{\dot{\Psi}}(\omega) \approx \Psi_\infty$ for the teleseismic frequencies is equivalent to assuming that the source appears to be a delta function of amplitude Ψ_∞ to a teleseismic observer.

equivalent to assuming that the source behaves, teleseis-
mically, as if it were a delta function of amplitude ψ_∞^e.
Computation of theoretical seismograms show that this assump-
tion is not bad. The value of $\dot{\hat{\psi}}^e$ is taken to be the value
of $\dot{\hat{\psi}}(\omega)$ at the frequency which cube root scales to the
yield of interest. With this modification, (A.5) is the
appropriate scaling law for the sources of Section IV in a
homogeneous earth model.

A Spherically Symmetric Source in a Two Layered Whole Space

Let us now assume that the spherically symmetric source
is located in a space composed of two layers. The geometry
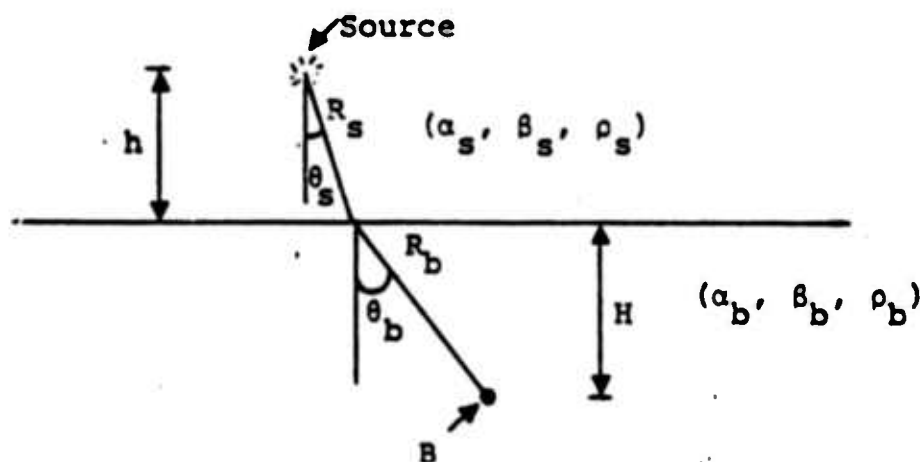is shown in Fig. A.1.

Figure A.1. A source in a two layered medium.

If attention is restricted to the far field, the
displacement in potential form is given by (A.4). Then the
P wave displacement at the point B below the interface is
given by

$$\hat{u}_b = \frac{A}{L} \frac{\dot{\hat{\psi}}(\omega)}{\alpha_s} e^{-i\omega\tau_b} , \qquad (A.6)$$

where

$$L^2 = \left(R_s + \frac{\alpha_b}{\alpha_s} R_b\right)\left(R_s + \frac{\cos^2\theta_s}{\cos^2\theta_b} \frac{\alpha_b}{\alpha_s} R_b\right),$$

$$A = \frac{2\rho_s\alpha_s}{D} P_1 \left(\beta_b P_2 X + \beta_s P_4 Y\right),$$

$$D = \alpha_s\alpha_b\beta_s\beta_b \frac{Z^2}{c^2} + \alpha_b\beta_b P_1 P_2 X^2 + \alpha_s\beta_s P_3 P_4 Y^2$$

$$+ \rho_s\rho_b \left(\beta_s\alpha_b P_1 P_4 + \alpha_s\beta_b P_2 P_3\right) + \frac{q^2}{c^2} P_1 P_2 P_3 P_4, \qquad (A.7)$$

$$X = \rho_b - \frac{q}{c^2}, \quad Y = \rho_s + \frac{q}{c^2}, \quad Z = \rho_b - \rho_s - \frac{q}{c^2},$$

$$P_1 = \cos\theta_s, \quad P_2 = \left(1 - \frac{\beta_s^2}{c^2}\right)^{1/2}, \quad P_3 = \cos\theta_b, \quad P_4 = \left(1 - \frac{\beta_b^2}{c^2}\right)^{1/2},$$

$$C = \frac{\alpha_s}{\sin\theta_s} = \frac{\alpha_b}{\sin\theta_b}, \quad q = 2\left(\rho_b\beta_b^2 - \rho_s\beta_s^2\right).$$

In (A.6) the exponential term is merely the phase shift due to the travel time from the source to B. The L is the spreading term for the spherical wave. For a homogeneous material, $L = R$, the distance between the source and B. The coefficient A is the refraction coefficient which depends on the properties of the two media and the angle of incidence which we denote θ_s.

Application to Teleseismic Body Waves

The two layered model of Fig. A.1 is more realistic than a homogeneous earth model for illuminating the gross

properties of the teleseismic body waves excited by explosions in different source materials. For example, consider the NTS explosions. The resulting teleseismic body waves observed at a single seismograph station are expected to vary due to differences only in the explosion source and near source crustal structure. All other features of the travel path are essentially held constant.

Below some depth one expects all of the NTS to be underlain by a common material. The material denoted by a subscript b can be thought of as this basement rock. Explosions at NTS have been detonated in such widely varying materials as alluvium, tuff, rhyolite and granite. These are characterized by P wave velocities ranging from 2.0 - 5.5 km/sec. The subscript s can be taken to represent this source material. For the long wavelengths (> 2 km) of interest for teleseismic waves, the single interface transition between the source and basement materials is a useful approximation.

The body waves reaching the teleseismic field exit the source region at near vertical takeoff angles. That is, $\cos\theta_s \approx 1$ and $\cos\theta_b \approx 1$. Then it is clear from (A.7) that

$$L \approx R_s + \frac{\alpha_b}{\alpha_s} R_b . \tag{A.8}$$

However, since the basement rock is held in common from event to event, one can choose R_b arbitrarily large while R_s remains rather small. Thus, comparing different events at NTS, $L \approx \alpha_b/\alpha_s$.

The complexity of its form makes it difficult to deduce a similarly simple relationship for A. However, numerical experiments using values for typical geologic materials and horizontal wave speed c (or takeoff angle θ_b) show that A is very nearly proportional to α_s/α_b. Taking c = 12 km/sec and α_b = 6.0 km/sec, β_b = 3.5 km/sec, ρ_b = 2.8 gm/cm³, a number of illustrative examples are given in Table A.1.

TABLE A.1. THE REFRACTION COEFFICIENT A FOR TYPICAL SOURCE
MATERIALS

α_s	β_s	ρ_s	θ_s	A	$\alpha_b A / \alpha_s$
2.40	1.30	1.86	11.53	0.4199	1.05
2.80	1.40	1.95	13.29	0.4906	1.05
3.30	1.90	2.25	15.66	0.6130	1.11
4.00	2.50	2.40	19.26	0.7273	1.09
4.50	2.65	2.60	21.71	0.8211	1.09
5.10	2.75	2.70	24.20	0.9009	1.06
5.50	3.10	2.75	26.74	0.9475	1.03

For short period teleseismic body waves $\hat{\dot{\Psi}}(\omega)$ may
be replaced by the constant Ψ_∞^e. Then combining all these
approximations with (A.6), we find that teleseismic amplitude
is proportional to $\alpha_s \Psi_\infty^e$. That is, for the two layered earth
model we deduce that

$$|u_t| \approx \alpha_s \Psi_\infty^e . \tag{A.9}$$

It should be emphasized that it is the direct P wave
that scales with $\alpha_s \Psi_\infty^e$. Extending this to scale m_b implicitly
assumes that the influence of the free surface reflected phase
and details of the near source geology are invarient between
events. The usefulness of (A.9) is degraded to the extent
that this is not true.

Calculation of the RDP

The RDP is calculated in the following manner. If we assume that the displacement is linear within a given time interval defined by

$$\tau_1 < \tau < \tau_2$$

then Eq. (A.2) gives

$$\Psi(\tau_2) = aR^2\left[\tau_2 - \tau_1 e^x\right] + R^2\left(b - \frac{aR}{\alpha_s}\right)\left[1 - e^x\right] + e^x\Psi(\tau_1) \quad (A.10)$$

where

$$a = \frac{u(\tau_1, R) - u(\tau_2, R)}{\tau_1 - \tau_2}$$

$$b = \frac{-u(\tau_1, R)\tau_2 + u(\tau_2, R)\tau_1}{\tau_1 - \tau_2}$$

$$x = \frac{\alpha_s(\tau_1 - \tau_2)}{R}$$

At late times when the displacement becomes constant, τ_2 can be much larger than τ_1 so that

$$e_x \to 0$$

$$a \to 0$$

$$b = u(\infty, R)$$

The steady-state value of the RDP becomes

$$\Psi(\infty) = R^2 u(\infty, R) \quad (A.11)$$

This result also follows directly from Eq. (A.2) since

$$\dot{\Psi}(\infty) = 0 \tag{A.12}$$

In an entirely analogous manner, the reduced velocity potential (RVP) may be computed from the velocity-time history of a particle. If $\dot{u}(t,R)$ is radial particle velocity, then

$$\dot{u}(t,R) = -\frac{\partial}{\partial R} \frac{\dot{\Psi}(\tau)}{R} = \frac{\dot{\Psi}(\tau)}{R^2} + \frac{\ddot{\Psi}(\tau)}{\alpha_s R} \tag{A.13}$$

where $\dot{\Psi}(\tau)$ is the RVP.

If $\dot{\Psi}(\tau)$ replaces $\Psi(\tau)$ and $\dot{u}(\tau,R)$ replaces $u(\tau,R)$ in Eq. (A.10), then the algorithm for calculating the RVP follows directly.

It is highly desirable to transform the equivalent source into the frequency domain in order to identify the frequency dependence of the spectrum required for equivalent source comparison. Since $\dot{\Psi}(\infty) = 0$, then $\dot{\Psi}$ is bounded at zero frequency and the Fourier transform of $\dot{\Psi}(\tau)$ may be done numerically.

An important relation is that the zero frequency limit of the RVP is equal to the steady state value of the RDP. Since

$$\hat{\dot{\Psi}}(f=0) = \int_0^\infty \dot{\Psi}(\tau) \, d\tau = \int_0^\infty \frac{d\Psi(\tau)}{d\tau} \, d\tau$$

Therefore, since $\Psi(0) = 0$,

$$\hat{\dot{\Psi}}(0) = \Psi(\infty) \tag{A.14}$$

Reduced velocity potentials have been computed for a variety of near source geologic environments. These calculations were performed on a Lagrangian finite difference code,

65

SKIPPER (see Appendix B), that simulates a propagating stress
wave in one space dimension. The difference equations in the
code are identical to those given by Cherry and Petersen.[7]
The code is capable of carrying the propagating stress wave
into the small displacement, elastic regime and yet flexible
enough to permit appropriate material response formulations
in the large displacement, nonlinear regime.

Figure A.2 shows $|\hat{\ddot{\Psi}}|$ versus frequency for a nuclear
explosion of 20 kt. Each source function in the figure is
identified by an integer and corresponds to a 20 kt explosion
detonated in a geologic environment with a specific set of
material properties given in Section III. For all practical
purposes the spectra are flat within the teleseismic
frequency band (f < 3 Hz) for yields up to at least 200 kt.
This implies that teleseismic body wave and surface wave ampli-
tudes should be directly proportional to the yield of the ex-
plosion. Deviation from this linear scaling should occur
within the yield interval 200 kt < W < 1,000 kt, depending on
the source function used to represent the rock material near
the source.

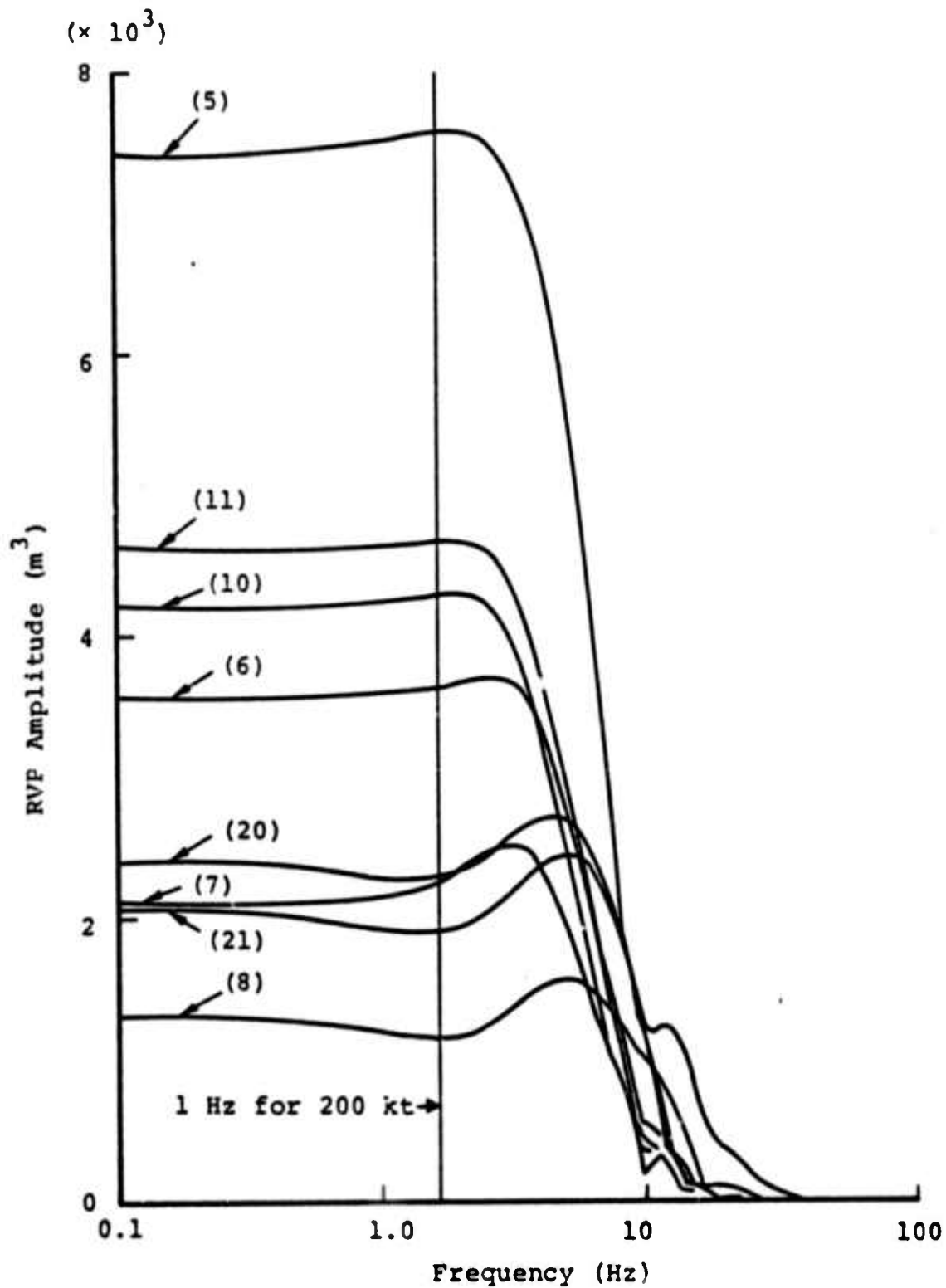Figure A.2. Source functions scaled to 20 kt.

APPENDIX B

THE SKIPPER CODE

B.1   DESCRIPTION OF THE CODE

SKIPPER is a Lagrangian, finite difference code that simulates a propagating stress wave in one space dimension. The code is capable of carrying the propagating stress wave into the small displacement, elastic regime and yet flexible enough to permit appropriate material response formulations in the large displacement, nonlinear regime.

A schematic of one computational cycle is shown in Fig. B.1. The equation of motion for spherical symmetry is

$$\rho \dot{u} = -\left[\frac{\partial \sigma_1}{\partial r} + \frac{2(\sigma_1 - \sigma_2)}{r} \right] \tag{B.1}$$

where ρ is density, u is particle velocity, $\dot{u}$ is particle acceleration and σ_1 and σ_2 are the radial and tangential components of the stress tensor with compression positive.

Strain rates in the radial and tangential direction are

$$\dot{\epsilon}_1 = \frac{\partial u}{\partial r} \tag{B.2}$$

$$\dot{\epsilon}_2 = \frac{u}{r} \tag{B.3}$$

The stress tensor may be decomposed into an isotropic component (P) and a deviatoric component (S_1 and S_2) where

$$\sigma_i = P - S_i \tag{B.4}$$
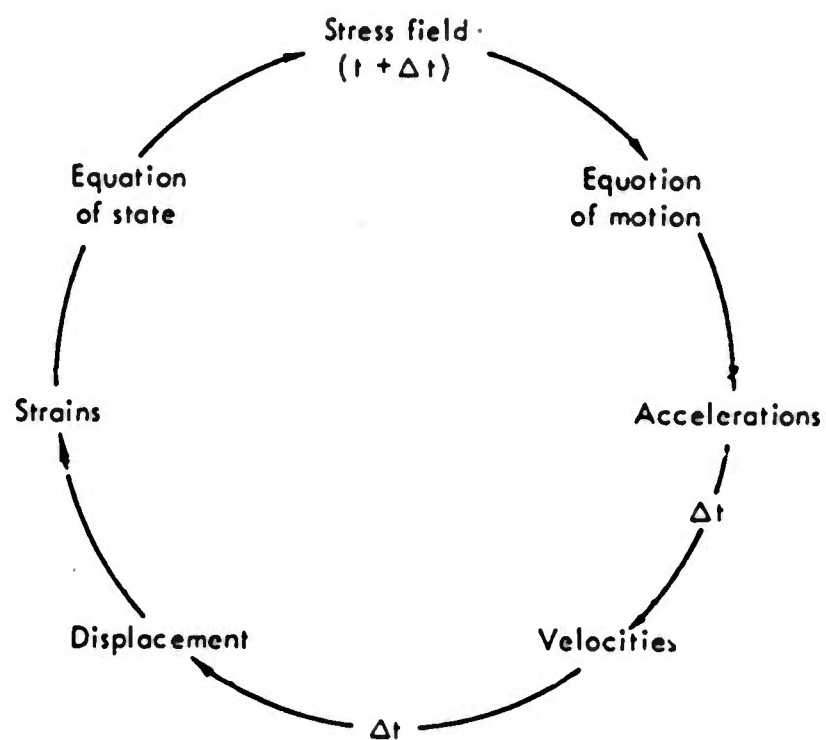
Due to symmetry

$$S_1 = -2S_2 \tag{B.5}$$

Figure B.1. Cycle of interactions treated in cal-
culating stress wave propagation. Taken
from Ref. 5.

Hooke's law gives

$$\dot{P} = -\kappa \frac{\dot{v}}{v} \tag{B.6}$$

$$\dot{S}_1 = \frac{4}{3} \mu (\dot{\varepsilon}_1 - \dot{\varepsilon}_2) \tag{B.7}$$

where k and μ are the bulk and shear moduli, the dot
indicates a time derivative along a particle path and from
conservation of mass the rate of change of volume is

$$\frac{\dot{v}}{v} = \dot{\varepsilon}_1 + 2\dot{\varepsilon}_2 \tag{B.8}$$

For large and/or energy dependent deformations Eq.
(B.6) is replaced by

$$P = f_1(v,e) \quad \text{or} \quad P = g(\bar{\eta}, e) \tag{B.9}$$

where v is specific volume.

The specific internal energy (e) is obtained from

$$\rho \dot{e} = -P \frac{\dot{v}}{v} + S_1 \dot{\varepsilon}_1 + 2S_2 \dot{\varepsilon}_2 \tag{B.10}$$

and the total volumetric strain $(\bar{\eta})$ is defined to be

$$\bar{\eta} = \frac{v^0 - v}{v^0} = 1 - \frac{v}{v_0} = 1 - \frac{\rho_0}{\rho} \tag{B.11}$$

The difference equation used in the code that corresponds to
Eqs. (B.1), (B.2), (B.3), (B.10) and (B.11) are the same as
those used by Cherry and Petersen.[7]

Basically, Eqs. (B.7) and (B.9) should be regarded as
an initial attempt by the code to determine P and S_1 at
the current time cycle. Modification of these stresses then
depend on the constitutive relation used in the equation of
state section of the code.

An artificial viscosity is used in the momentum and energy equations [(B.1) and (B.10)] and has the same form as that reported by Wilkins.[8] This quantity replaces discontinuous jumps in particle velocity in the calculation with a rapid but continuous change.

B.2   SKIPPER COMPARISON TO AN ANALYTIC SOLUTION

Normally, the only way to evaluate a numerical procedure is to examine its ability to produce the answer to a previously solved problem. Also, in order to calculate the equivalent elastic source function from a contained nuclear explosion, the calculations must be continued well into the small displacement, elastic regime. In order for the calculation to be meaningful in this regime the numerics in the code must not introduce errors in the solution when displacements are small.

A well-known analytic solution, commonly called Blake's solution,[9] to an elastic wave propagation problem has been used for our analytic comparison. The following parameters were used in the calculation:

Cavity Radius	≈ 10 meters
Density	= 2 g/cc
Compressional Velocity	= 5 m/msec
Bulk Modulus	= 333.33 kbar
Shear Modulus	= 125 kbar
Cavity Load (kbar)	= e^{-t} (t in msec)
Zone Size	= 10 cm

Figures B.2 and B.3 show particle velocity versus radius at 1.32 msec and 6.81 msec. Figures B.4 and B.5 show displacement and mean stress versus time 10 m from the cavity wall.

The numerical results from SKIPPER agree quite well with the analytic solution. Displacement time histories of the type shown in Fig. B.4 provide the input for the RDP calculation.
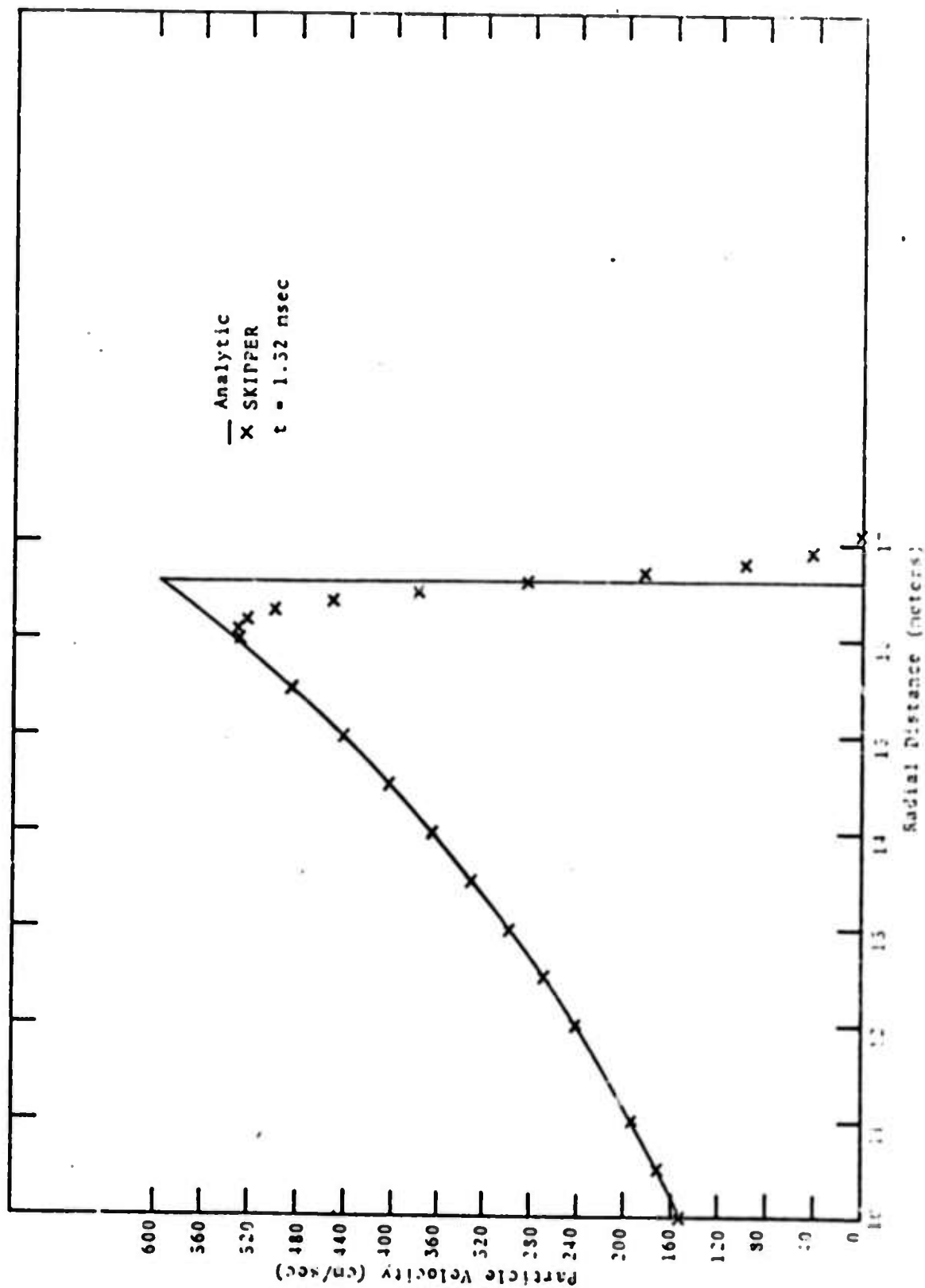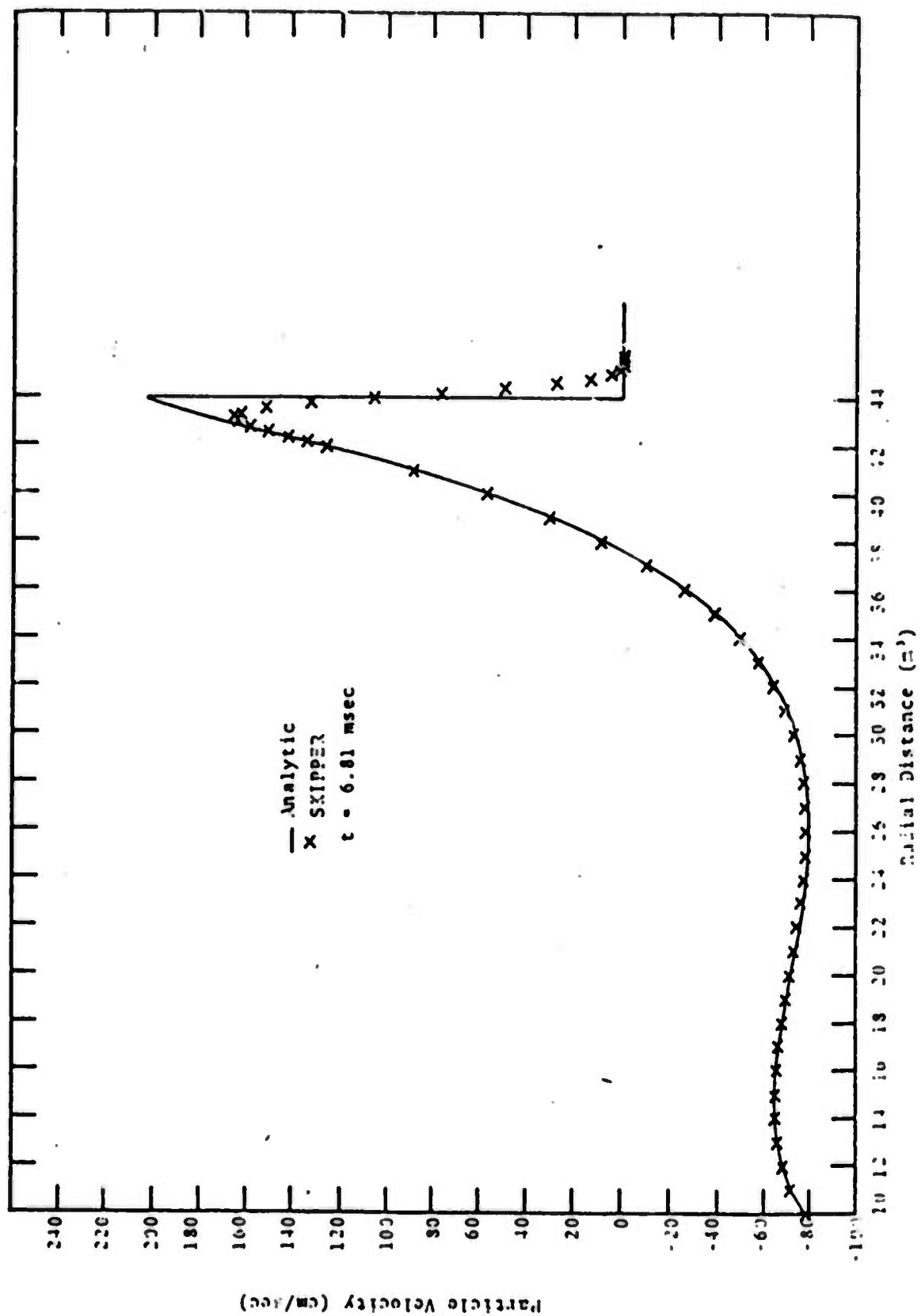
Figure B.2. SKIPPER – analytic comparison.

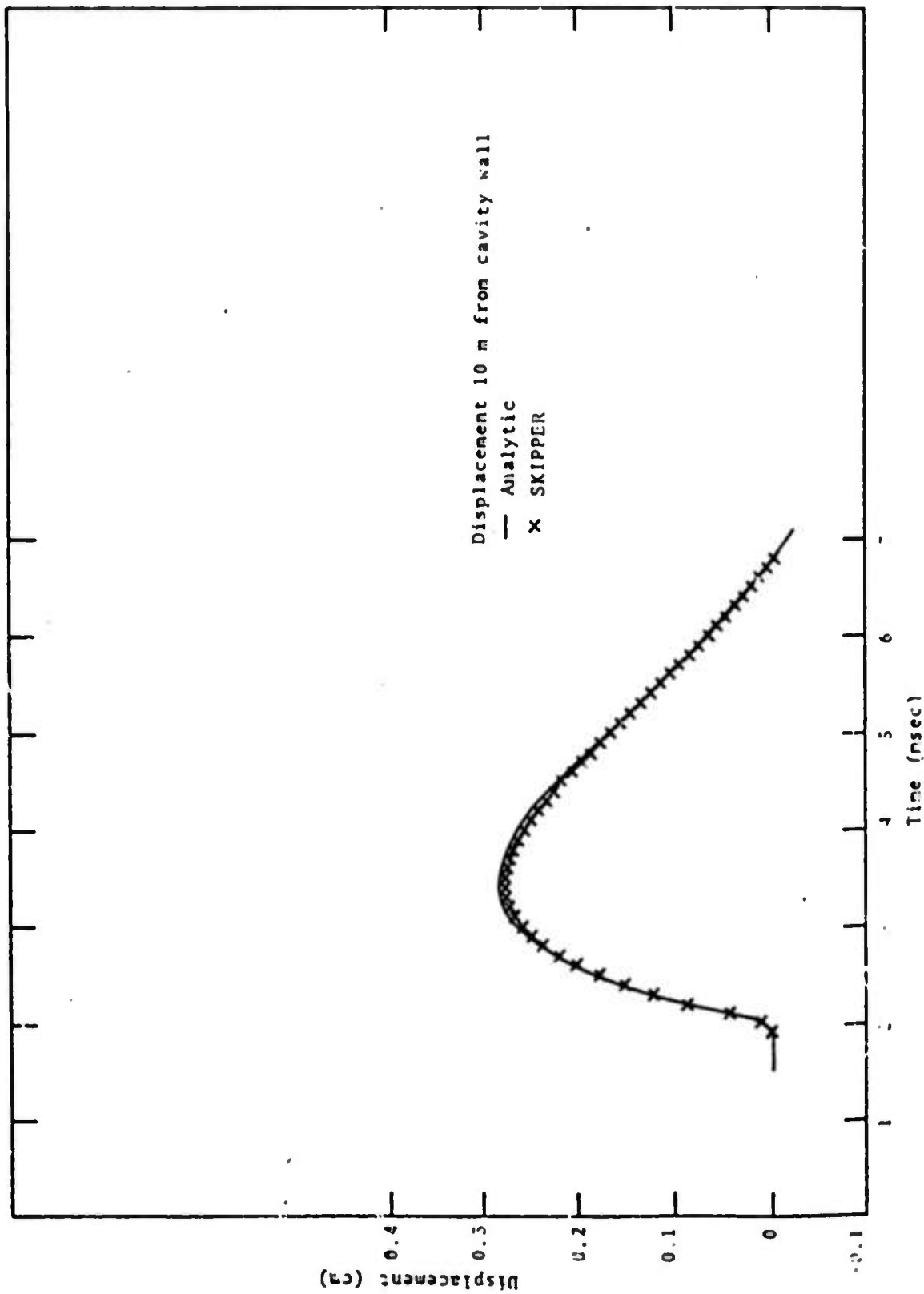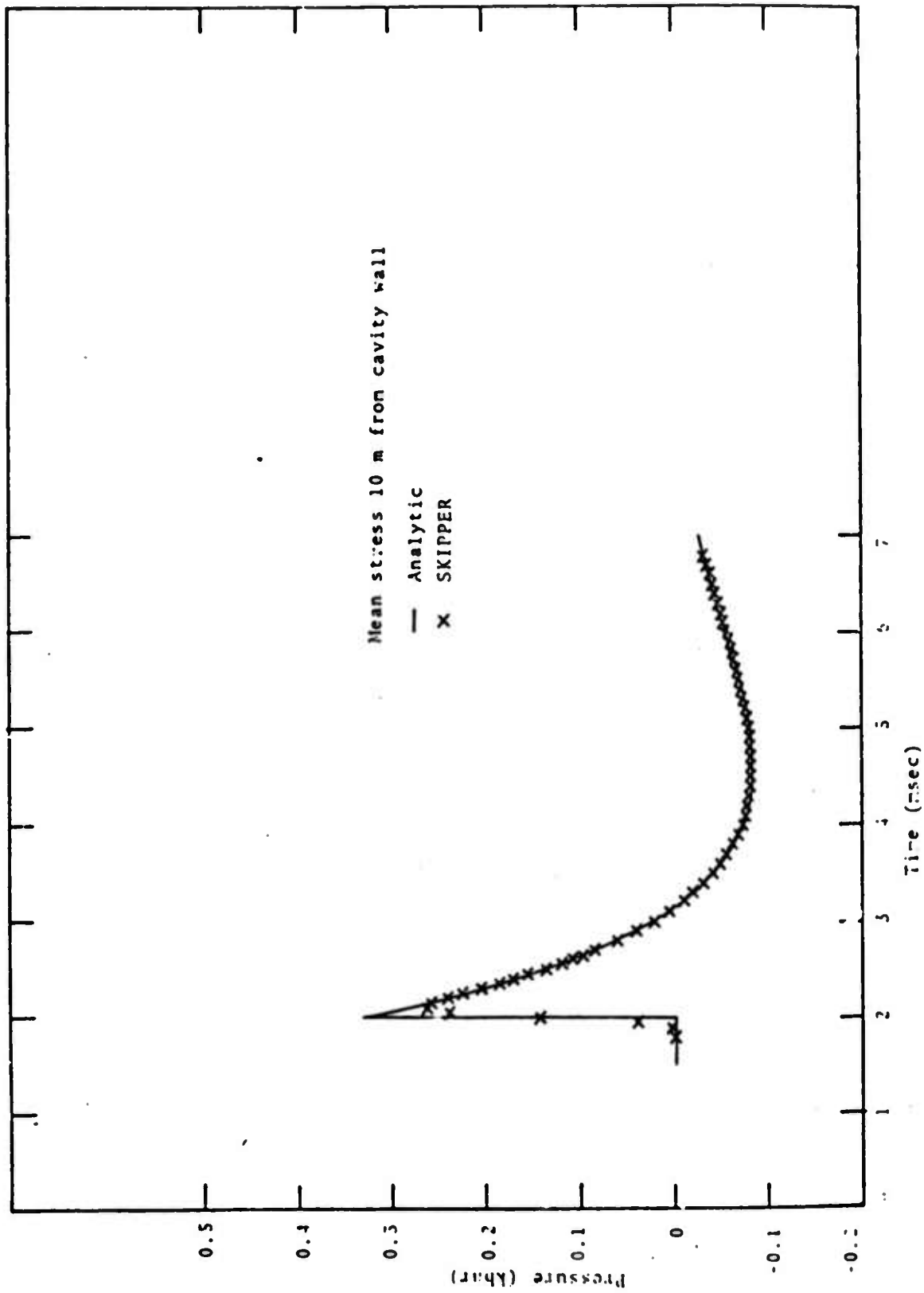Figure B.3. SKIPPER - analytic comparison.

Figure B.4. SKIPPER - analytic comparison.

Figure B.5. SKIPPER – analytic comparison.